This is a non-peer reviewed preprint submitted to EarthArXiv, The manuscript was submitted for review in *Sedimentology*.

Carbonate polymorphism controlled by microbial iron redox dynamics at a natural CO_2 leakage site (Crystal Geyser, Utah)

JULIE COSMIDIS[1,2], SHANE O'REILLY[3,4], ERIC T. ELLISON[1], KATHERINE L. CRISPIN[5], DAVID DIERCKS[6] and ALEXIS S. TEMPLETON[1]

[1]*Department of Geological Sciences, University of Colorado, Boulder, CO 80309, USA*

[2]*Department of Earth Sciences, University of Oxford, Oxford OX1 3AN, UK*

[3]*School of Earth Sciences, University College Dublin, Belfield, Dublin 4, Ireland*

[4]*Institute of Technology Sligo, Sligo F91 YW50, Ireland*

[5]*Materials Research Institute, Pennsylvania State University, University Park, PA 16802, USA*

[6]*Department of Metallurgical and Materials Engineering, Colorado School of Mines, Golden, CO 80401, USA*

Corresponding author: Julie Cosmidis. Email: julie.cosmidis@earth.ox.ac.uk

ABSTRACT

Crystal Geyser (Utah, USA) is a CO_2-rich low-temperature geyser that is studied as a natural analog for CO_2 leakage from carbon capture and storage (CCS) sites. In order to better constrain the biogeochemical processes influencing $CaCO_3$ precipitation at geological CO_2 escape sites, we characterized fast-forming iron-rich calcium carbonate pisoids and travertines precipitating from the fluids expelled by the geyser. The pisoids, located within a few meters from the vent, are composed of concentric layers of aragonite and calcite. Calcite layers contain abundant ferrihydrite shrubs in which iron is encasing bacterial forms. The aragonite layers contain less abundant and finely dispersed iron, present either as iron-oxide microspherules or iron adsorbed to organic matter dispersed within the carbonate matrix. We propose that carbonate polymorphism in the pisoids is mostly controlled by local fluctuations of the iron redox state of the fluids from which they form, caused by episodic blooms of iron-oxidizing bacteria. Indeed, the waters expelled by Crystal Geyser contain >200 µM dissolved iron (Fe^{2+}), a known inhibitor of calcite growth. The calcite layers of the pisoids may record episodes of intense microbial iron oxidation, consistent with observations of iron-oxide rich biofilms thriving in the rimstone pools around the geyser and previous metagenomic analyses showing abundant neutrophilic, microaerophilic iron-oxidizing bacteria in vent water. In turn, aragonite layers of the pisoids likely precipitate from Fe^{2+}-rich waters, registering periods of less intense iron oxidation. Separately, $CaCO_3$ polymorphism in the travertines, where calcite and aragonite precipitate concurrently, is not controlled by iron dynamics, but may be locally influenced by the presence of microbial biofilms. This study documents for the first time an influence of microbial iron oxidation on $CaCO_3$ polymorphism in the environment, and informs our understanding of carbonate formation at CO_2 leakage sites and in CCS contexts.

Keywords

Travertines, pisoids, carbonates, CCS, iron oxidation, frutexites

INTRODUCTION

Carbon Capture and Storage (CCS) are climate mitigation technologies whereby carbon dioxide (CO_2) is captured at large emission sources (e.g., fossil fuel power plants or industrial sites), and injected into deep sedimentary reservoirs for long-term storage. These negative carbon emission strategies are essential tools to meet global climate goals (van Vuuren *et al.*, 2017) but several challenges and uncertainties are still limiting their application (Kelemen *et al.*, 2019). Among them, the potential for CO_2 stored in deep aquifers to leak to the surface along natural fractures or through injection wells and boreholes is of particular concern (Alcalde *et al.*, 2018).

Naturally occurring as well as man-made CO_2 leakage sites have been studied to understand the fate and impact of geological CO_2 in surface environments (e.g., Lewicki *et al.*, 2006; Roberts & Stalker, 2017). Crystal Geyser (Utah, USA) is an abandoned petroleum exploration well, drilled in 1935, from which CO_2 has been leaking to the surface for decades at a pace of ~12 kt/yr (Gouveia *et al.*, 2005). The well bore reaches a deep CO_2-charged aquifer in the Navajo Sandstone (Colorado Plateau), from which CO_2 has also been leaking along natural faults for more than 400,000 years (Shipton *et al.*, 2004; Burnside *et al.*, 2013). CO_2 at Crystal Geyser is escaping to the surface both as free gas and dissolved in brines expelled during eruptions (Assayag *et al.*, 2009; Kampman *et al.*, 2014). It is estimated that 1 to 10% of the dissolved CO_2 is precipitated as calcium-carbonates (travertines), forming a mound around the geyser (Shipton *et al.*, 2004; Burnside *et al.*, 2013).

Here, we performed a detailed characterization of travertines and pisoids forming at Crystal Geyser, in order to identify chemical and biological processes influencing $CaCO_3$ precipitation, with a particular focus on $CaCO_3$ polymorphism. Various efforts have been made to constrain the physicochemical factors influencing the polymorphism of calcium carbonates precipitating from CO_2-rich springs. Parameters such as temperature, pH, CO_2 content and degassing rate, fluid ionic strength, and presence of sulfate, metals cations, and organics, determine whether calcite, aragonite, or (more rarely) vaterite, may form in CO_2-rich spring systems (Chang *et al.*, 2017; Jones, 2017). In addition, biological factors such as the presence of microbial cells and extracellular polymeric substances (EPS) may also influence $CaCO_3$ polymorphism in travertines (Guo & Riding, 1992; Okumura *et al.*, 2013a; b; Peng & Jones, 2013). Parameters controlling $CaCO_3$ polymorphism at CO_2 leakage sites need to be constrained to improve our understanding of the fate and long-term stability of carbon trapped as carbonate minerals. Moreover, understanding the processes influencing the precipitation, polymorphism, and physicochemical properties of $CaCO_3$ formed in CO_2 storage settings participates in efforts aimed at valorizing $CaCO_3$ as value-added materials for different industries (construction materials, food and pharmaceuticals, paper, etc.), potentially offsetting the cost of CCS (Chang *et al.*, 2017).

This work combines mineralogical and chemical characterizations of the travertines and pisoids at Crystal Geyser, geochemical analyses of the fluids from which they form, and investigations of microbe-mineral interactions through microscopy and lipid biomarker analyses, in order to better constrain physicochemical and biological processes impacting $CaCO_3$ mineralization and polymorphism at CO_2 leakage sites. An influence of microbial iron oxidation on $CaCO_3$ polymorphism in a CO_2-rich environment is shown here for the first time, a process that may be important in CCS contexts.

BACKGROUND

Setting: Crystal Geyser

Crystal Geyser is a cool CO_2-driven geyser located 14.5 kilometers southeast of the town Green River in Utah (USA). Its hydrology has been described elsewhere (Shipton *et al.*, 2004; Gouveia *et al.*, 2005; Gouveia & Friedmann, 2006; Assayag *et al.*, 2009; Heath *et al.*, 2009; Wilkinson *et al.*, 2009; Han *et al.*, 2013; Kampman *et al.*, 2014), and a brief summary will be given here. Crystal Geyser waters erupt from an abandoned exploration well drilled in 1935 (a pipe, standing ~2 m above the ground, was added for safety in the 1990s). The well was drilled into 21.5 m of pre-existing travertines, showing the existence of natural springs at this location prior to drilling (Baer & Rigby, 1978). Although the drill-hole is ~800 m deep, erupted waters discharge predominantly from the Jurassic Navajo Sandstone at ~200-350 m depths. Crystal Geyser erupts mildly reducing (Eh ~ -5 mV), slightly acidic (pH ~6.5), cold waters (~18 °C), containing mixtures of groundwater of meteoritic origin (80-90% of erupted waters) and brines emanating from deeper (~1.5 km depth) carboniferous evaporite formations (~10-20 % of erupted waters) (Wilkinson *et al.*, 2009; Kampman *et al.*, 2014). Crystal Geyser erupts CO_2 both as a free gas (representing ~96% of the erupted gases; Kampman *et al.*, 2014) and dissolved in the waters (which start degassing at ~120 m depths as the waters migrate vertically in the drill-hole; Assayag *et al.*, 2009). The CO_2 emanates from carbonate dissolution by acidic groundwater in the Navajo sandstone (Heath *et al.*, 2009) and deep supercritical CO_2 reservoirs migrating upwards through a normal fault system (Shipton *et al.*, 2004; Gilfillan *et al.*, 2008).

The intensity of Crystal Geyser eruptions has been declining with time since the drilling of the oil well at its origin. In 1973, the discharge from a single eruption was measured to be ~120 m^3, while in 2001 the discharge was only ~25 m^3 (Waltham, 2001). The frequency and duration of eruption is also evolving with time. Earlier publications have reported a bimodal eruption cycle, with large eruptions lasting between 1 and 1.5h (Type B) and 5-7h (Type D), occurring every 7-10 h or 20-30 h, respectively (Gouveia *et al.*, 2005; Gouveia & Friedmann, 2006; Han *et al.*, 2013). Between these large eruptions, smaller magnitude “bubbling events” (Type A and C eruptions; Han *et al.*, 2013) would occur approximatively every 15 minutes. However, longer duration (~24 h) and lower frequency (every ~70 h) eruptions have been described by Kampman *et al.* (2014) who observed the geyser in 2012. For the present study, Crystal Geyser was visited in 2014, and a short (1-2 hours) eruption event was observed followed by continuous “bubbling” lasting approximatively 24 hours. After this, the geyser and surrounding pools were totally dry for ~24 hours. During the following ~24 hours, the pool directly around the geyser vent was observed to be slowly filling with water flowing from holes at the base of the pipe, after which another eruption/bubbling event started. In 2015, Crystal Geyser was visited for a few hours on two consecutive days. On the first day, the geyser was observed to be “bubbling”, while on the following day no water was flowing from the geyser and its surroundings were dry.

During eruptions, Crystal Geyser waters flow towards Green River, located ~80 m downstream. Along their flow path, the waters deposit terraced travertines which form a gently sloping mound with a lateral extent of ~85 m (Barth & Chafetz, 2015). The travertines are bright red in color directly around the vent of the geyser and become orange and yellow more distally. Brighter colors are observed centrally respective to the water flow path, and paler colors laterally (Fig. 1A,G). Green mats, likely corresponding to algae and cyanobacteria (Takashima *et al.*, 2011b; Barth & Chafetz, 2015), cover the central portion of the travertines in the warm season (Fig. S1A,B).

During eruptions, pools around the geyser fill with water, which can be flowing or stagnant depending on the timing and intensity of the eruptions. When waters are stagnant, rusty materials (most likely iron-(oxyhydr)oxides) form at the surface of the pool directly surrounding the geyser (Fig. 1D), while oily-looking films are observed at the surface of shallow rimstone pools located slightly further downstream. Between eruptions, the area surrounding geyser dries up completely (Fig. 1C).

The modern travertine (deposited since the drilling of the oil well bore in 1935) is estimated to be ~1 m (Burnside *et al.*, 2013) to several meters (Barth & Chafetz, 2015) thick, corresponding to sedimentation rates of more than one to several centimeters per year. Fast carbonate precipitation at Crystal Geyser is also evidenced by the presence of recently encrusted plants and objects across the field site (Figs. S1J,K).

Crystal Geyser travertines and pisoids

Crystal Geyser terraced travertines form a gently sloping mound around the geyser. Near Green River, the slope abruptly becomes steeper and the travertines form staircase-like steps (Fig. 1G). The travertines are often laminated (Fig. 1H), which was interpreted as resulting from daily banding combined with the eruption pattern of the geyser (with dark, micritic bands, influenced by photosynthetic organisms, forming when both sunlight and water are available, and lighter bands with larger crystals developing at night when water is present) (Takashima *et al.*, 2011b). Some travertines furthermore display microstromatolitic horizons, interpreted as resulting from the encrustation of microbial mats (Barth & Chafetz, 2015). Travertines located downslope or laterally respective to the water flow path are often more porous, and may contain fenestrae-like holes and include calcified bubbles (Fig. 1I). Crystal Geyser travertines contain iron-

(oxyhydr)oxides which give them their red to orange colors (depending on iron abundances). The iron-(oxyhydr)oxides sometimes form filaments and hollow tube-like structures, interpreted as encrusted sheaths of iron-oxidizing bacteria (Barth & Chafetz, 2015). At the surface of the travertines, calcium carbonates frequently form fan-shaped bundles of feather-like crystals, eventually producing botryoidal structures, previously interpreted as being microbial in origin (Parenteau & Cady, 2010; Barth & Chafetz, 2015). Large (> 1 cm) botryoidal, cauliflower-shaped carbonate structures we also observed at the surface of the travertines in pools located distally from the vent of the geyser (Figs. S1C-E). Other botryoidal structures shaped like toroids were also found (Fig. S1F). They could possibly form around calcified gas bubbles which are frequently observed in the rimstone pools (Fig. S1G-I). These botryoidal structures will not be further described here.

Reddish pisoids (*i.e.*, rounded coated grains measuring less than a centimeter in diameter) accumulate in rimstone pools mostly located proximal to the geyser (Fig. 1F). Small pisoids are typically simple and well-rounded, while larger ones can be complex (composed of multiple aggregated smaller coated grains) and irregularly shaped. The nuclei of the pisoids often contain quartz grains cemented by calcium carbonates (Barth & Chafetz, 2015). Their cortices are formed by alternating layers of calcium carbonate and iron. Iron-(oxyhydr)oxides frequently form outwardly branching growth patterns, or “shrubs”, resembling frutexites, which are often interpreted as fossil microbial structures (Takashima *et al.*, 2008; Jakubowicz *et al.*, 2014; Guido *et al.*, 2016; Reitner *et al.*, 2017; Grădinaru *et al.*, 2020). Due to their proximity to Crystal Geyser’s vent, Barth and Chafetz (2015) proposed that the pisoids may be formed within the geyser's plumbing system and ejected during eruptions. Analyses were focused on these pisoids due to their potential to probe $CaCO_3$ formation in the subsurface.

MATERIALS AND METHODS

Sample collection

Crystal Geyser was visited in April 2014 and February 2015. Samples of the pisoids (found within ~10 m of the geyser) and two different types of travertine were collected: a visibly laminated travertine (Fig. 1H), referred to hereafter as TL, and a non-laminated, porous travertine containing calcified gas bubbles (Fig. 1I), referred to hereafter as TB. Both travertines were collected distally from the geyser, in the area where travertines form steep slopes towards the river (Fig. 1G). Water samples were also collected from Crystal Geyser's vent for geochemical analyses during eruptions or "bubbling" events. Particles from erupted waters were collected by filtration on 0.2 µm polycarbonate filters. The filters were rinsed immediately with deionized water and air-dried, and preserved for later mineralogical analyses.

Water chemistry

Major cations (Mn^{2+}, Fe^{2+}, Mg^{2+}, Ca^{2+}, Al^{3+}, Sr^{2+}, Na^+, K^+) and SiO_2 were analyzed on water samples collected from Crystal Geyser's vent in 2014 and 2015. The water samples were filtered and acidified in the field, and cations were analyzed using Inductively Coupled Plasma-Mass Spectrometry (ICP-MS) on a ThermoScientific X Series 2. Major anions (F^-, Cl^-, Br^-, NO_2^-, NO_3^-, PO_4^{3-}, SO_4^{2-}) were analyzed on field-filtered samples collected in 2014 only. Anion analyses were performed using Ion Chromatography (IC) on a Dionex IC25 with an IonPac column and a 9 mM sodium carbonate eluent.

Profiles of dissolved Fe(II) and total Fe (measured by colorimetry) were obtained across the field site using a portable Hach DR890 instrument in 2014. pH and temperature were measured with a separate Hach multimeter with a pH probe.

X-ray diffraction

Samples of the pisoids and travertines TB and TL were finely ground with an agate mortar and pestle, and the powders were analyzed using a Bruker D2 Phaser operated at 30 kV and 10 mA. X-ray diffraction (XRD) spectra were obtained in the 2θ range 10-65° using Cu Kα radiation (λ = 1.5418Å) and a Lynxeye 1D detector with a step size of 0.02° and collection time of 1 s per step.

X-ray absorption spectroscopy

X-ray absorption spectroscopy at the Fe K-edge was performed to determine iron speciation in the travertines and pisoids. Samples were ground to a fine powder using an agate mortar and pestle, and loaded into sample folders sealed with kapton tape. X-ray absorption spectroscopy measurements were performed on beamline 4-1 of the Stanford Synchrotron Radiation Lightsource (SSRL). X-ray absorption spectra were collected in fluorescence mode using a Si (220) $\phi = 0$ monochromator and a Lytle detector Energy was calibrated by setting the first inflection point of the Fe K-edge XANES spectrum of a reference Fe^0 foil to 7112 eV. Two to four spectra were collected and averaged for each sample. X-ray absorption near edge structure (XANES) spectra were background subtracted and normalized to unit step edge using the SIXPack software package (Webb, 2005). Extended X-ray absorption fine structure (EXAFS) spectra were extracted with SIXPack using a threshold energy of 7125 eV. Previously published spectra of 2-Line ferrihydrite, hematite, goethite (Maillot *et al.*, 2011) and lepidocrocite (Pantke *et al.*, 2012) were used for comparison with the samples.

Raman spectromicroscopy

Raman spectra and hyperspectral maps were acquired on thin sections of the pisoids and travertines, as well as on particles from Crystal Geyser's vent waters collected on polycarbonate filters. The analyses were performed using a Horiba LabRAM HR Evolution Raman spectrometer using a 532 nm frequency-doubled Nd:YAG laser and a Si-based CCD detector (1024 x 256 pixels). The laser beam was focused through a 10x or 50x objective lens, yielding a spatial resolution of ~5 µm or ~2 µm respectively. Spectra were collected from 80 to 1800 cm^{-1}. A spectral resolution full width at half maximum (FWHM) of 4.5–8.4 cm^{-1} was obtained using a 600 lines/mm grating and adjustable confocal pinhole (100–200 µm). Prior to analysis, calibration of the spectrometer was performed using the 520 cm^{-1} Raman peak of Si. Spectral data were corrected for instrumental artifacts and baseline-subtracted using a polynomial fitting algorithm in LabSpec 6 (Horiba Scientific). Raman maps were used to visualize the distribution of mineral species using least-squares fitting. Spectra were averaged over a small portion of the map containing relatively pure Raman spectra in order to define end-members. These end-members were then used to fit the full map dataset by classical least squared constrained by non-negativity of the fit coefficients using LabSpec 6 (Horiba Scientific).

Electron microprobe

Electron probe microanalyses (EPMA) were performed on a polished thin section of a pisoid. The EPMA maps were collected on a CAMECA SX-Five microprobe using a LaB6 source at 15kV, 15nA with the beam defocused to 5 µm diameter. The stitched images are a mosaic composed of 3x3 individual maps, collected at 256x256 pixels, with a step size of 10 µm and dwell time of 25 ms per pixel. All elements were collected using the Kα x-ray line except Lα for

Sr. A LTAP crystal was used to collect Mg, and Al. A PET crystal was used to collect Ca, S, Si, K, and P. A LPET crystal was used to collect Sr. A LLIF crystal was used to collect Fe. Energy-dispersive X-ray spectroscopy was used to collect C and O.

Scanning Electron Microscopy

Scanning Electron Microscopy (SEM) was performed on different types of pisoid samples: (i) polished pisoid cuts, (ii) pisoid cuts etched with HCl, and (iii) thin sections. SEM analyses were also performed on particles from Crystal Geyser vent waters collected on polycarbonate filters. All samples were coated with gold prior to SEM. The analyses were conducted on a JSM-7401F field emission SEM. Images were acquired in the secondary electron mode with the microscope operating at 5 kV and a working distance of 6 mm, and in the backscattered electron mode at 10 kV and a working distance of 10 mm. Elemental analyses and maps were obtained using Energy-dispersive X-ray spectroscopy (EDX), performed at 20 kV with a working distance of 8 mm.

Focused Ion Beam

Specimens from a pisoid were prepared for Transmission Electron Microscopy (TEM) in an FEI Helios NanoLab 600i Ga focused ion beam / scanning electron microscope (FIB/SEM) using an in-situ lift-out method. Electron beam assisted deposition of Pt from a Trimethyl(methylcyclopentadienyl)platinum(IV) source was used as an initial protective layer over the regions of interest. This was followed by ion beam assisted deposition from the same source to a total of ~ 2 µm thickness. An ion beam accelerating voltage of 30 kV was used to mill around the regions of interest and for thinning of the specimens after they had been extracted to a TEM grid by a nanomanipulator. Final thinning of the specimens was performed using a 2kV ion beam accelerating voltage. Locations of the two FIB sections performed in the pisoid are depicted in Figures S2 and S3.

Transmission Electron Microscopy

TEM analysis of the FIB sections was performed on an FEI Talos F200X instrument using a 200 keV accelerating voltage. Analyses included bright field and dark field imaging, high angle annular dark field scanning TEM (HAADF-STEM) imaging, selected area diffraction, and EDX compositional mapping. The EDX data were processed using Bruker Esprit 1.9 software.

Scanning Transmission X-ray Microscopy

Scanning Transmission X-ray Microscopy (STXM) was performed on FIB sections 1 and 2 on beamline 10ID-1 (SM) of the Canadian Light Source (Saskatoon, Canada) (Kaznatcheev *et al.*, 2007). Energy calibration was achieved using the 3p Rydberg peak of gaseous CO_2 at 294.96 eV. Images, maps and image stacks were obtained at the C K-edge, the Ca $L_{2,3}$-edge, and Fe $L_{2,3}$-edges, using a 25 nm zone plate. STXM data was processed using the aXis2000 software (Hitchcock, 2012). Organic carbon maps were obtained by subtracting an image at 280 eV (pre-edge) and converted into an optical density (OD) image, from an OD-converted image at 288.5 eV (energy of the $1s \rightarrow \pi^*$ electronic transition in carbonyl and carboxylic groups). Carbonate maps were obtained by subtracting an OD-converted image at 280 eV (pre-edge) from an OD-converted image at 290.2 eV (energy of the $1s \rightarrow \pi^*$ electronic transition in carbonate groups). Calcium maps were obtained by subtracting an OD-converted image at 342 eV (pre-edge) from an OD-converted image at 349.2 eV (energy of the Ca L_3-edge main peak). Iron maps were obtained by subtracting an OD-converted image at 700 eV (pre-edge) from an OD-converted image at 710.2 eV (energy of main absorption peak in Fe-(oxyhydr)oxides). Pixels with negative values in resulting maps were removed using the Clip Signal tool of aXis2000. XANES spectra where extracted from aligned image stacks as described in Cosmidis & Benzerara (2014). Linear background corrections were applied to the spectra in the 270-282 eV energy range at the C K-edge, in the in the 330-345 eV energy range at the Ca $L_{2,3}$-edges, and in the 690-704 eV energy range at the Fe $L_{2,3}$-edges. For some image stacks, representative XANES spectra for major components of the samples were extracted, and the relative contribution of these representative spectra at each pixel was mapped using the Stack Fit tool of aXis2000.

Lipid biomarkers

Lipid biomarkers were extracted from pisoid and travertine samples and analyzed using gas chromatography-mass spectrometry (GC-MS). 20.0 g of Crystal Geyser pisoids and travertines (TL and TB) were powdered using a shatterbox and accurately weighed into 60 mL glass centrifuge tubes. Each sample was spiked with 1 µg of nonadecan-1-ol internal standard. Samples were extracted with organic solvent as follows: 2:1 (v/v) methanol/dichloromethane (×3), followed by 9:1 (v/v) dichloromethane/methanol (×3). For each extraction, the tubes were sonicated for 10 minutes in an ultrasonic bath at room temperature. Extracts were separated from solid residues by centrifugation, and supernatants from each step were combined to give a total free lipid fraction, comprising surface and intercrystalline lipids. This fraction is referred to as the free lipid fraction. 10.0 g of the extracted residues were subsequently diluted in dichloromethane-cleaned water and carefully dissolved in HCl. When there was no evidence of remaining carbonate, lipids were extracted from the aqueous solutions using liquid-liquid extraction (dichloromethane, ×3). Lipids adsorbed to remaining residue were also extracted using sonication/centrifugation as described above, and combined to give a carbonate-bound (intracrystalline) lipid fraction.

All extracts were concentrated to minimal volume under a gentle stream of high purity N_2. A portion of each extract was then subjected to acid methanolysis (0.5 N methanolic HCl, 60°C ~10 h), followed by silylation (BSTFA (+1% trimethylchlorosilane) in pyridine, 70°C, 2 h). Derivatized samples were analyzed by gas chromatography-mass spectrometry (Agilent 5890 GC hyphenated to an Agilent 5975C Mass Selective Detector). The GC was equipped with a Gertsel programmable temperature vaporizer (70°C ramped to 360°C at a rate of 720°C min^{-1}) and a J&W 60 m capillary column (0.25 mm inner diameter, 250 μm film thickness). The GC temperature program was: 70°C for 2 min, ramp at 10°C min^{-1} to 130°C, followed by a ramp to 300°C at 4°C min^{-1} and a final hold time of 20 min. The mass spectrometer was operated in electron impact ionization mode (70 eV), with a mass scan range from m/z 50 to 600. All solvents used were high-purity (OmniSolv) and all aqueous solutions were cleaned with dichloromethane prior to use, and procedural blanks were run to monitor background contamination. The peak areas of analytes were compared with peaks of the internal standard and can be considered semi-quantitative.

RESULTS

The geochemical environment at Crystal Geyser

Table 1 shows concentrations of major elements measured in waters collected from the vent of the geyser on two different days in April 2014, as well as in February 2015. Crystal Geyser waters are rich in chloride, sodium, sulfate, calcium, potassium, and magnesium (in order of decreasing abundance), consistent with a contribution from brines originating from deep evaporite formations (Wilkinson *et al.*, 2009; Kampman *et al.*, 2014). Dissolved iron values measured by ICP-MS were 6.14-10.61 mg.L^{-1}, falling between the range of values reported by other authors (12.8-15.7 mg.L^{-1} in Kampman *et al.* (2014) and ~3.4 mg.L^{-1} in Heath *et al.* (2009)). Most of this dissolved iron is present under a reduced form, since colorimetric measurements performed on vent water during an eruption in 2014 showed 10.05 mg.L^{-1} Fe^{2+} and only 10.85 mg.L^{-1} total iron. Fe^{2+} in the geyser waters likely results from the reductive dissolution of hematite minerals present in the Navajo sandstone reservoir by CO_2-charged brines (Kampman *et al.*, 2014).

According to previous studies, Crystal Geyser waters are supersaturated with respect to both aragonite and calcite (Heath *et al.*, 2009). However, SEM and Raman analyses of vent particles collected on filters showed the presence of numerous aragonite blades (Fig. S4) and no calcite. Fine-grained iron minerals were also present, but it is not clear whether they originated from the geyser or if they precipitated on the filters from oxidation of Fe^{2+}-rich vent water during sample preparation.

Geochemical profiles of dissolved Fe(II), total Fe, pH, and temperature were obtained on-site in April 2014, using measurements performed at different locations along the geyser's flow path, from the pool around the vent to Green River (Fig. 2). The waters expelled by Crystal Geyser have temperatures of ~17-18 °C and pH values of ~6.5. As they flow towards Green River, they get progressively warmer (~24 °C at the river) and slightly more basic (pH ~7.8 at the river). This pH increase is consistent with progressive CO_2 degassing. Dissolved Fe(II) (Fe^{2+}) and total Fe (Fe_{tot}) concentrations decrease with distance from the vent, showing the progressive oxidation and precipitation of iron from the water.

Mineralogical description of the Crystal Geyser travertines and pisoids

Bulk mineralogical composition

Both aragonite and calcite were identified by XRD in the travertine samples TL and TB as well as in the pisoids (Fig. 3A). Fe K-edge EXAFS was used to determine the mineralogical composition of the iron-bearing phases giving the travertines and pisoids their orange color. EXAFS spectra match that of a ferrihydrite reference (Fig. 3A) (with possibly a slightly more disordered structure in the travertine samples as compared with the pisoids). The samples' spectra were fitted with reference spectra of different iron-(oxyhydr)oxides using a linear combination-least squares fitting approach. Two-line ferrihydrite provided the best fit for all samples, and no additional mineral improved the quality of the fits.

Mineralogical mapping

Raman spectromicroscopy was used to map the distribution of different mineral phases in the samples. In travertine TL, distinct microlaminae dominated by either aragonite or calcite can be found, although both phases are present in all microlaminae (Fig. 4). Quartz grains were also found in travertine TL; it is possible that these quartz grains were undetected by XRD due to their low abundance relative to calcium carbonates. Travertine TB is composed of randomly distributed aragonite and calcite grains, ranging from a few microns to ~100 μm in size (Fig. 5), with distinct areas of the travertine displaying different relative proportions of aragonite and calcite grains (compare Figs. 5D and 5G). The cortices of the pisoids are composed of concentric alternating layers of calcite and aragonite, measuring a few hundred micrometers in thickness (Fig. 6,S5,S6). Interestingly, the nuclei of all the pisoids analyzed (n = 5) contain aragonite as the main $CaCO_3$ phase, along with quartz grains. Some quartz grains were also found in the cortices of the pisoids. Ferrihydrite was not mapped with Raman, due to its typically weak signal, but Fe-rich regions were visible as red or brown areas on micrographs acquired along the maps. In all pisoids, ferrihydrite is mostly present in well-delimited layers spatially co-located with calcite (whereas aragonite layers are ferrihydrite-free). This co-occurrence between iron minerals and calcite was not observed in the travertine samples, where iron phases are more dispersed and finely intermixed with the carbonates.

Elemental mapping of a pisoid

Using EPMA, chemical maps showing the distribution of different elements in one Crystal Geyser pisoid were obtained (Fig. 6C-E, Fig. S7). Fe is mostly present in the cortex, as discrete layers of ferrihydrite co-located with calcite. Mg is particularly abundant in the nucleus of the pisoid, while in the cortex it appears only in calcite layers (Fig. 6D). Sr is distributed more homogeneously through the nucleus and cortex, with a slight enrichment in aragonite phases (Fig. S7). S is absent from the nucleus, and in the cortex it is preferentially associated with calcite (Fig. 6E). Si is found in hot spots, particularly abundant in the nucleus, and co-located with high abundances of oxygen (Fig. S7), consistent with the presence of quartz grains. Al, and K, sometimes with Mg, co-occur with some Si hot spots, likely corresponding to clay minerals (undetected with other methods) in both the nucleus and the cortex.

Nano-scale mineralogical characterization of a pisoid

Mineralogical and chemical characterization

Two FIB sections from a pisoid were analyzed using TEM and STXM (Figs. 7,8). The FIB sections were performed in porous areas of the cortex (Figs. S2,S3), in an attempt to sample and characterize trapped organic materials (see following section). These areas correspond to aragonitic layers of the cortex, as confirmed by electron diffraction (data not shown) and STXM/XANES analyses at the Ca $L_{2,3}$-edge (Fig. S8). Distinct aragonite crystals are visible on STXM carbonate maps (Fig. 7H, 8F), with sizes in the micrite range or smaller (< 2 µm). Although SEM and Raman analyses have shown that aragonitic layers of the pisoids contain only minor amounts of Fe, iron was found in both FIB sections, predominantly in an oxidized form (Fe(III)) based on XANES analyses at the Fe $L_{2,3}$-edge (Fig. S9). In FIB section 1, iron forms dense spherules, ~1-2 µm in diameter (Fig.7B,I). Several spherules form an aggregate near the top of the central part of the section. Iron also forms a circular structure, creating a broken ring around carbonates (near the top left corner of the section). High resolution TEM and SAED analyses show that the spherules are composed of nanocrystalline, 2-line ferrihydrite (Fig. 7E,F). Iron is present in a porous area of FIB section 2 (Fig. 8B,G), either as fine silicate particles (most likely clays) or as coatings of quartz grains, visible as Si-rich particles on EDX maps.

Organic matter distribution and characterization

Organic matter, mapped using STXM analyses at the C K-edge, is found concentrated around ferrihydrite spherules, or dispersed in the porosity of the aragonite matrix (Fig. 7G,8E). Organic matter around the ferrihydrite spherules is visible on TEM images of FIB section 1 showing an amorphous light material accumulating in the space between the spherules and the carbonate matrix (Fig. 7D). This organic matter has a composition similar to that associated with the protective platinum layer deposited on top of the FIB sections, suggesting that the organics present in the spaces around the ferrihydrite spherules were most likely introduced during the FIB milling process (“contamination” spectrum in Fig. 7M). C K-edge XANES spectra of this contaminating organic matter, also present in porous areas of the aragonite matrix at the top of the foils just below the platinum layer, are dominated by peaks at 284.9 eV (1s→π* transitions in aromatic C=C groups and unsaturated carbon), 288.6 eV (1s→π* transitions in carboxylic groups), 290.3 eV (1s→π* transitions in carbonate groups) and 292.4 eV (1s→σ* transitions in aromatic C-C groups), and a small shoulder at 286.1 eV (1s→π* transitions in carbonyls or phenols) (Brandes *et al.*, 2004; Schumacher *et al.*, 2005; Lehmann *et al.*, 2009). This composition matches that of organics present in the platinum covering the FIB foils (resulting from the decomposition of an organometallic precursor), dominated by aromatic groups (Carlut *et al.*, 2010; Cosmidis *et al.*, 2013), with the additional contribution of carbonates originating from aragonite matrix. On the other hand, C K-edge XANES spectra obtained on organic matter found dispersed in other areas of both FIB foils (Fig. 7L) have no or weak absorption signal from aromatics, and sometimes display additional peaks at 287.4 eV (1s→3p/σ* transitions in aliphatic carbon) (Brandes *et al.*, 2004; Lehmann *et al.*, 2009), not present in the spectra of the platinum layer organics, and indicating that this organic matter is most likely endogenous. C K-edge spectra of the aragonite grains are dominated by an intense peak at 290.3 eV (carbonate groups), consistent with its mineralogical composition, but also present a peak at 288.6 eV, which could be due to a change in bonding environment around the carbon atoms of the crystals (Brandes *et al.*, 2010), or to the presence of finely intermixed organics dominated by carboxylic groups.

Evidence for microbe-mineral interactions in the pisoids

Morphological evidence for microbial influences in calcium carbonate and iron precipitation

Ferrihydrite-rich layers of the pisoids display “shrub” textures, also called “frutexites” (Fig. 9A,B). Fractured pisoids etched with HCl were imaged with SEM (Fig. 9C-F). Etching dissolves away the surface of the carbonate matrix, revealing the internal structure of the ferrihydrite shrubs (Fig. 9C). Iron forms cavities with sub-spherical, rod-shaped or filamentous shapes (Fig. 9D-F). These cavities have internal diameters ranging from 0.5 to 2 μm and are interpreted as casts of microbial cells. Similar looking iron-rich “honeycomb” textures were depicted in ancient carbonate spring deposits and interpreted as microbial fossils (Potter-McIntyre *et al.*, 2017). Preserved microbial shapes were also visible in the carbonate matrix of the pisoids, forming either empty casts (Fig. 9G) or carbonate-filled molds (Fig. 9H,I), generally with larger dimensions (>5 μm), and possibly corresponding to entombed microalgae.

Lipid analyses

A detailed description of free and carbonate-bound lipid biomarkers extracted from Crystal Geyser’s pisoids and travertines can be found in the Supplementary Materials (Table S1, Supplementary Text). Total lipid abundances are low overall, reflecting the low abundance of organic carbon in the carbonates by mass. The carbonate-bound lipid fraction of the travertine TB yields 4x lower lipid concentration than the pisoids and travertine TL. Fatty acids are the major lipid components detected in all samples but significant variation between each sample type and free and bound fractions are observed (Fig. 10). The ratio of bound: free fatty acids is 4.1:1 for the pisoids, 1.4:1 for travertine TL and 1:4.3 for travertine BL. This confirms the higher abundance of microbial organic matter in the pisoids and travertine TL compared with travertine TB. It is not possible to identify the source of all fatty acids as many, especially *n*-saturated and monounsaturated, are common to bacteria and eukaryotes (Table S1). However, the presence of *iso*- and *anteiso*- branched saturated and 3-hydroxy acids indicates a strong contribution from anaerobic bacteria (Kaneda, 1991; O’Reilly *et al.*, 2017). *n*-alkanols (notably, the unusual nonacosan-12-ol and hentriacontan-12-ol), β-sitosterol and stigmasterol (both C_{29} sterols) and odd-carbon-number long chain ($>C_{23}$) alkanes were also present in the free lipid fractions of all samples, indicating the presence of vascular plants (most likely from eolian input) and photosynthetic microalgae (forming visible mats the surface of the travertines) (O'Reilly *et al.*, 2017, and references therein). Archaeol occurs in high relative abundance in the free lipid fraction of the pisoids, and is absent from the travertine samples. This confirms the presence of archaea as major clades in microbial communities in the growth environment of the pisoids (Kate, 1993), a finding that is consistent with the detection of abundant archaea in Crystal Geyser vent waters as determined by metagenomic and lipid analyses (Probst *et al.*, 2014, 2017, 2020).

DISCUSSION

Origin of Crystal Geyser pisoids

Pisoids are coated grains larger than 2 mm displaying concentric internal layering in a cortex growing around a central nucleus. Carbonate pisoids and smaller coated grains (ooids) are frequent in marine environments, but have also been described in travertine settings (Kano *et al.*, 2019; Della Porta *et al.*, 2021). Although small and irregularly shaped ooids (<1 mm) have recently been shown to form *in-situ* within microbial mats (Suarez-Gonzalez & Reitner, 2021), coated grains usually thought to indicate growth while rolling in flowing water. At Crystal Geyser, the pisoids may have formed in two distinct types of settings: either at the surface in pools where water is flowing during large eruptions, or in the subsurface in the borehole where water is turbulent during eruptions and “bubbling” events. The pisoids are mostly found in the vicinity of Crystal Geyser's vent, with larger pisoids occurring closer to the vent, and smaller ones are found more distally. For these reasons, Barth and Chafetz (2015) proposed that the pisoids may be formed within the plumbing system of the geyser, and ejected during eruptions. The nuclei of the pisoids often contain abundant quartz grains, a major component of the sandstone formation from which Crystal Geyser's waters originate, as well as cementing calcium carbonates. In all pisoids analyzed with Raman, aragonite was the only $CaCO_3$ phase identified in the nuclei (Figs. 6,S5,S6). Aragonite is also the carbonate structure found in all carbonate particles filtered out of the waters expelled from Crystal Geyser's vent (Fig. S4), suggesting that the nuclei of the pisoids were formed under similar geochemical conditions as these particles, i.e. in the subsurface. The nuclei of the pisoids are furthermore relatively free of iron and sulfur (Fig. 6C,E), suggesting that they formed under reducing conditions. Indeed, in the presence of oxygen, Fe^{2+} dissolved in the water would oxidize and precipitate as Fe(III) phases which would be incorporated in the pisoids during growth (as observed in the cortices). Similarly, in the presence of oxygen, sulfide (which is also present in the water as evidenced by the characteristic sulfide smell at the vent of the geyser) would oxidize as sulfate which is readily incorporated into carbonates. Thus, absence of S and Fe in the nuclei of the pisoids, along with the presence of these elements in their cortices, demonstrates initial formation under reducing conditions followed by further growth in more oxidizing conditions. The fact that at least some pisoid growth occurs above ground is furthermore evidenced by the presence of lipid biomarkers for higher plants and microalgae in the carbonate-bound fraction of pisoids. Overall, results thus support an initial formation of the pisoids in the subsurface in Crystal Geyser's plumbing system, with some further growth after ejection at the surface.

The precipitation of $CaCO_3$ minerals composing the pisoids is likely mostly driven by degassing of CO_2-rich waters, either in the subsurface while fluids migrate vertically during eruptions and “bubbling”, or in pools at the surface. Although a primarily abiotic process, microbial influences on $CaCO_3$ mineralization in the pisoids are reflected in the high proportion of bound fatty acids in these objects (Fig. 10), and the presence of microorganisms encased in the carbonate matrix (Fig. 9G,I). Barth and Chafetz (2015) described carbonate spherulites, formed by aragonite crystals radiating from central clumps of bacteria-shaped objects, in the nuclei of some Crystal Geyser pisoids. These objects are usually interpreted as resulting from carbonate nucleation on microbial cells and their EPS (Chafetz *et al.*, 2018). Influences on $CaCO_3$ precipitation by microbial activity and EPS was documented in marine coated grains (Diaz *et al.*, 2015, 2017), but the results obtained here on the Crystal Geyser pisoids do not allow to determine whether similar mechanism are at play here.

Calcium carbonate polymorphism and iron redox dynamics in the pisoids

Carbonate polymorphism in CO_2-rich spring systems is a complex, multi-parameter problem, and may be influenced by a great number of geochemical and biological factors including water temperature, pH, CO_2 content and degassing rate, calcium carbonate saturation state, the presence of sulfate, metals and divalent ions, organics substances, and microbial mats (Chang *et al.*, 2017; Jones, 2017). The pisoids at Crystal Geyser are particularly interesting due to a clear relationship between carbonate polymorphism and iron behavior. Indeed, their cortices are composed of alternating layers of aragonite and calcite, suggestion shifting (bio)geochemical conditions during pisoid growth. While calcite layers contain abundant iron, forming ferrihydrite shrubs, aragonite layers contain only minor amounts of iron, present as ferrihydrite spherulites or iron associated with clays, quartz grains, and organics (Figs. 6,7,8). Different hypotheses to explain this correlation are discussed here.

Iron control on $CaCO_3$ polymorphism in Crystal Geyser's pisoids

A first hypothesis is that iron behavior exerts a direct control on $CaCO_3$ polymorphism in the pisoids. Numerous experiments have shown that Fe^{2+} is an inhibitor of calcite growth (Meyer, 1984; Gutjahr *et al.*, 1996; de Leeuw, 2002; Mejri *et al.*, 2015), promoting the precipitation of aragonite over calcite. In Crystal Geyser's plumbing system, where the pisoids are thought to start forming, dissolved iron (Fe^{2+}) is present at relatively high concentrations (values ranging from 3.4 to 15.7 $mg.L^{-1}$ have been measured by ourselves and others at the vent; Table 1; Heath *et al.*, 2009; Kampman *et al.*, 2014). The inhibitory effect of Fe^{2+} on calcite formation would explain why the nuclei of the pisoids (as well as particles present in vent water) contain exclusively aragonite. At the surface, the pisoids grow in rimstone pools proximal to the geyser, where Fe^{2+} is still present (conditions similar to site 2 Fig. 2), favoring aragonite formation. Ferrihydrite-rich layers in the cortices of the pisoids show that Fe^{2+} is episodically oxidized (a process that may be biologically mediated – see next section), causing Fe(III) precipitation. The resulting local decrease in dissolved Fe^{2+} in the pools would remove calcite inhibition and allow the formation of the calcitic layers of the pisoids. In some layers, calcite seems to precipitate before ferrihydrite starts to form (see for instance the outermost calcite layer on top of Fig. 6A). However, it is possible that ferrihydrite incorporation in the growing pisoids occurs with a delay compared to Fe^{2+} oxidation in solution. Indeed, observations of rusty materials as well as oily-looking films (often attributed to iron-oxidizing bacteria; Dyer, 2003) at the surface of stagnant pools around the geyser (Fig. 1D,E) indicate that following Fe^{2+} oxidation, Fe(III)-phases do not immediately sink to the bottom of the pools.

Competing hypotheses for $CaCO_3$ polymorphism in the pisoids

Although the model depicted above, based on iron redox dynamics and calcite inhibition by Fe^{2+}, satisfactorily explain mineralogical observations reported in this study, competing hypotheses need to be considered to account for the correlation between $CaCO_3$ polymorphism and iron behavior in Crystal Geyser pisoids. It could be proposed that $CaCO_3$ polymorphs directly control iron behavior. Experiments have shown that calcite has a catalytic effect on iron oxidation, with Fe(II) adsorption at the surface of calcite grains accelerating the rate at which it is oxidized to Fe(III) in the presence of oxygen (Mettler *et al.*, 2009). However, aragonite most likely has a similar catalytic effect on iron oxidation. It is thus unlikely that $CaCO_3$ polymorphism directly controls iron oxidation and distribution.

Since at least part of the pisoids growth occurs in the plumbing system of the geyser, it is necessary to consider the potential impact of physicochemical fluctuations in the subsurface on carbonate polymorphism. These fluctuations are mostly driven by the eruption cycle of the geyser (Kampman *et al.*, 2014; Han *et al.*, 2017). The temperature and pH of the geyser waters are relatively constant over time and through the eruption cycle, with temperature variations smaller than 3.5 °C (ranging from 15.5 to 18.8 °C) and pH variations smaller than 1.5 units (ranging from 6.2 to 7.6), as measured by several authors (Baer & Rigby, 1978; Shipton *et al.*, 2004; Assayag *et al.*, 2009; Heath *et al.*, 2009; Takashima *et al.*, 2011b; Kampman *et al.*, 2014; Emerson *et al.*, 2016; Han *et al.*, 2017). Temperature favorizes aragonite precipitation at values greater than 35 °C, and the influence of pH on $CaCO_3$ polymorphism is relatively insignificant compared with other chemical parameters except at pH values higher than 10 (Chang *et al.*, 2017; Jones, 2017). It thus seems unlikely that variations in Crystal Geyser's water temperature and pH may be driving $CaCO_3$ polymorphism in the pisoids. Similar to the effect of Fe^{2+}, the presence of magnesium (as Mg^{2+} ions) in solution inhibits calcite growth and promotes aragonite precipitation. The Mg/Ca ratio appears to be particularly important for controlling $CaCO_3$ polymorphism (with higher ratios favoring the precipitation of aragonite over calcite) (Lin & Singer, 2009). Mg/Ca molar ratios in Crystal Geyser's waters measured by ourselves (Table 1) and others (Kampman *et al.*, 2014; Han *et al.*, 2017) are remarkably constant around 0.37 (± 0.01), and variations of this parameter over time are thus unlikely to be the cause of changes in $CaCO_3$ polymorphism at this site. The presence of strontium is also a factor favoring aragonite precipitation over calcite (Jones, 2017). Sr variations in Crystal Geyser's waters are relatively wide (~127-220 µM; Kampman *et al.*, 2014; Han *et al.*, 2017). However, EPMA analyses show constant concentrations of Sr across aragonite and calcite layers of a pisoid (Fig. S7), therefore Sr probably do not control $CaCO_3$ polymorphism. The presence of sulfate in solution is known to selectively inhibit calcite growth (Walter, 1985), especially in the presence of Mg^{2+} (Nielsen *et al.*, 2016). However, Han *et al.* (2017) measured that SO_4^{2+} concentrations in Crstal Geyser vent waters vary by less than 15% through several eruption periods, suggesting that sulfate fluctuation in the subsurface probably do not affect $CaCO_3$ polymorphism in the pisoids.

CO_2 degassing rate is an important factor likely to vary dramatically over an eruption cycle of the geyser. Aragonite precipitation is thought to be favored over calcite in waters with high CO_2 degassing rates (Holland *et al.*, 1964; Jones, 2017). This effect is consistent with the presence of aragonite in the nuclei of the pisoids, forming within the plumbing system of the geyser, where

CO_2 content and degassing rates (due to turbulent mixing during the vertical migration of the fluid) are high. However, a model where CO_2 degassing rate is the main driver or $CaCO_3$ polymorphism cannot account for calcite and Fe(III) co-precipitation in the pisoids. Indeed, intense CO_2 degassing correlates with periods of water-air mixing during eruptions or “bubbling”, i.e. turbulent events that are also likely to cause Fe^{2+} oxidation and Fe(III) precipitation. Thus, if CO_2 degassing were the main driver for $CaCO_3$ polymorphism in the pisoids, ferrihydrite would be mostly co-located with aragonite layers rather than calcite.

Physicochemical changes that may be occurring in the rimstone pools where (at least some of) the pisoid growth is occurring should now be considered. Unfortunately, geochemical parameters in pools were not measured in time series. However, an indication of the changes that may affect Crystal Geyser water once at the surface is shown by the geochemical profile in Figure 2. Depending on air temperature, the temperature of the water in the pools may increase with time, but it is not likely to reach the values (well above 35 °C) where it affects $CaCO_3$ polymorphism. Similarly, pH is unlikely to show dramatic changes after a slight increase (by less than 1.5 pH units) due to CO_2 degassing. No data on the evolution of Mg, Sr, SO_4^{2-}, or other species likely to affect the structure of precipitating $CaCO_3$ in pools, has been acquired. However, the correlation between $CaCO_3$ polymorphism and iron distribution in the pisoids suggest that what controls shifts from aragonitic to calcitic conditions is probably a redox-active process. Iron is experiencing dramatic changes at the surface due to oxidation (Fig. 2), as also shown by changes in the visual aspect of the pools (Fig. 1D,E). Sulfate is also likely to improve with time in the pools due to oxidation of reduced sulfur species. However, increases in SO_4^{2-} concentrations should favor aragonite formation over calcite. If sulfur oxidation in surface pools was controlling

$CaCO_3$ polymorphism, periods of pool water oxygenation and consecutive Fe(IIII) formation would correspond to the precipitation of aragonite layers. Since the opposite correlation is observed, sulfate variations can be ruled out as an important factor in $CaCO_3$ polymorphism. It can be concluded that $CaCO_3$ polymorphism in Crystal Geyser pisoids is mostly controlled by iron redox dynamics, either in the subsurface or in surface pools where the pisoids are growing.

Microbial iron oxidation in the pisoids formation environment

As noted by Kappler *et al.* (2021), in the presence of oxygen, iron oxidation by biotic and abiotic pathways typically occur in parallel, making it challenging to identify the occurrence and quantitative contribution of iron-oxidizing bacteria to overall Fe(II) oxidation. Shiraishi *et al.*, (2018) showed that both microbial and abiotic iron oxidation may account for ferrihydrite deposition in spring systems, depending on fluctuations of the water oxygen concentration. However, several lines of evidence suggest that ferrihydrite in Crystal Geyser's pisoids is at least in part a product of microbial iron oxidation, either at the subsurface in pools, or in the subsurface in the plumbing system of the geyser. Oily-looking, iridescent films developing in stagnant pools after eruptions (Fig. 1E) are a typical signature of microaerophilic iron-oxidizing bacteria (Dyer, 2003; Fru *et al.*, 2012). Neutrophilic microaerophilic iron-oxidizing bacteria dominate microbial diversity in Crystal Geyser's vent water (Emerson *et al.*, 2016), including *Mariprofundus* (Zetaproteobacteria), and several members of the Gallionellales (Betaproteobacteria), such as *Gallionella* and *Sideroxydans*. Iron oxidizers of the genera *Mariprofundus* and *Galionella* produce recognizable extracellular structures forming ribbon-like, twisted stalks composed of Fe-(oxyhydr)oxides and organic polymers (Chan *et al.*, 2011, 2016), which were not found in the pisoids. However, ferrihydrite in the iron-rich layers of the pisoids forms “honeycomb” microtextures, encasing sub-spherical, rod-shaped or filamentous shapes with sizes ranging from 0.5-2 µm (Fig. 9D-F), interpreted as iron-encrusted microbial cells (Potter-McIntyre *et al.*, 2017). The encrusted cells may correspond to iron-oxidizers of the genus *Sideroxydans* or other members of the *Gallionellales* which precipitate extracellular Fe-(oxyhydr)oxides not associated with any stalks or other recognizable extracellular structures (Emerson & Moyer, 1997; Weiss *et al.*, 2007; Fleming *et al.*, 2014). The overall texture of the ferrihydrite layers of the pisoids furthermore corresponds to what has been described as iron shrubs (Chafetz *et al.*, 1998; Chafetz & Guidry, 1999; Takashima *et al.*, 2008; Parenteau & Cady, 2010) or frutexites (Jakubowicz *et al.*, 2014; Guido *et al.*, 2016; Reitner *et al.*, 2017; Grădinaru *et al.*, 2020) (Fig. 9A,B), and which are commonly interpreted as microbial in origin. Of particular relevance here, upward-branching iron shrubs described by Takashima *et al.* (2008) in laminated travertines forming at the Shionoha hot spring (Japan) are composed of ferrihydrites encrusting rod-shaped structures produced by microaerophilic iron-oxidizers of the genus *Siderooxidans*. Shrub-like dendritic iron-oxide structures associated with Gallionellaceae were also described in carbonates forming from CO_2- and iron-rich circumneutral hot springs at Okuoku-hachikurou Onsen (Japan) by Ward *et al.* (2017). In other hot spring laminated travertines (Ilia Hot Spring, Greece), iron shrubs are associated with iron-oxidizing Zetaproteobacteria (Kanellopoulos *et al.*, 2019). Iron shrubs can also be formed by microorganisms other than microaerophilic iron-oxidizers. For instance, in microbial mats forming in iron-rich hot springs (Chocolate Pots, Yellowstone National Park), iron shrubs are produced by cyanobacteria such as *Oscillatoria*, *Synechococcus,* and *Cyanothece* encrusted with ferrihydrite (Trouwborst *et al.*, 2007; Parenteau & Cady, 2010).

The iron-rich layers in Crystal Geyser pisoids may thus record changes in the abundance and activity of neutrophilic microaerophilic iron-oxidizers, episodically precipitating Fe(III). Abundances of these microorganisms can fluctuate in the environment due to a number of physicochemical factors that may include availability of complex organic carbon, iron abundance, and the steepness of the redoxcline (Fleming *et al.*, 2014; Blackwell *et al.*, 2019). At Crystal Geyser, the eruption cycle is likely to be an important factor controlling variations in the abundance and activity of iron-oxidizing bacteria. At the surface, iron-oxidizers may bloom after each eruption of the geyser, introducing reduced iron from the subsurface. In the subsurface, iron-oxidizers may be active during eruptions of bubbling events when turbulent mixing introduces oxygen in water.

In iron-poor (aragonitic) layers of the pisoids, iron is present as ferrihydrite spherules (Fig. 7), Fe(III) in clays and coatings of quartz grains, but also associated with organic matter found in the porosity of the carbonate matrix (Fig. 8). Fe(III) has a strong affinity for organic matter, adsorbing on negatively charged functional groups such as carboxylates or phosphorylates (González *et al.*, 2014), and frequently forms organo-ferric colloids in the environment (Ilina *et al.*, 2016; Liao *et al.*, 2017). The origin of the ferrihydrite microspherules is more enigmatic. Since they are included in the aragonite matrix, they are likely to have formed in solution prior to $CaCO_3$ formation. The presence of some space between the spherules and the carbonates (where contaminating organic matter could accumulate during the FIB milling process; Fig. 7D,K,M), suggests some shrinking after their incorporation within the aragonite matrix. Spheroidal ferrihydrite particles were observed to form aggregates around bacteria in iron-rich laminated carbonate spring deposits (Takashima *et al.*, 2011a) but an abiotic origin for the ferrihydrite microspherules in the Crystal Geyser pisoids cannot be discounted.

Microbial influences on $CaCO_3$ precipitation and polymorphism in Crystal Geyser travertines

Evidence for microbial influence on travertine formation

Travertine formation at Crystal Geyser is most probably a primarily abiotic process resulting from CO_2 degassing. It is unclear what impact microbial activities may have on the intensity of $CaCO_3$ precipitation in such CO_2-rich environment. However, microbial influences on $CaCO_3$ mineralization have been documented for many travertine systems (Shiraishi *et al.*, 2008; Perri *et al.*, 2012; Okumura *et al.*, 2013a; Kano *et al.*, 2019; Della Porta *et al.*, 2021), producing recognizable sedimentary fabrics and textures (Guo & Riding, 1992; Kano *et al.*, 2019). In Crystal Geyser travertines, such microbial influences are thought to be responsible for lamination, microstromatolitic horizons, and other features such as botryoidal carbonate textures (Takashima *et al.*, 2011b; Barth & Chafetz, 2015). Lipid analyses have shown abundant bound fatty acids in the laminated travertines (TL), while most lipids in the non-laminated travertine (TB) were free (Fig. 10). This difference may indicate more important contributions of microorganisms to $CaCO_3$ precipitation in travertine TL, as compared with travertine TB, in agreement with the absence of lamination in the latter sample. However, the presence of fenestrae and calcified bubbles in travertine TB (Fig. 5A) indicates gas formation concurrent with $CaCO_3$ precipitation, possibly resulting from microbial activity (e.g., O_2 production by aerobic phototrophs; Bosak *et al.*, 2010; Della Porta *et al.*, 2021).

Origin of $CaCO_3$ polymorphism in the travertines

Iron oxidation is not likely to be important factor controlling $CaCO_3$ polymorphism in the travertines, which are formed at a distance from the geyser, where the well-oxygenated waters are Fe^{2+}-poor (conditions similar to site 3 in Fig. 2). Ferrihydrite is present at relatively low abundances (compared with the pisoids) and there is no correlation between iron distribution and $CaCO_3$ polymorphism in the travertines. Aragonite and calcite are concentrated respectively in different microlaminae of travertine TL, but both phases can be found together in each microlaminae. In travertine TB, grains of both aragonite and calcite are found together in the same areas (Figs. 4,5). Small-scale variations of $CaCO_3$ polymorphism in the travertines probably results from localized physicochemical changes occurring in micro-environments at the surface of the growing travertines, most likely under the influence of microorganisms and their EPS. Peng & Jones, (2013) described the co-precipitation of calcite, aragonite and amorphous calcium carbonate within distances of a few microns in hot spring deposits. They proposed that microbial biofilms growing on the carbonates were forming microdomains, within which specific physicochemical conditions developed as a result of microbial activity, influencing $CaCO_3$ precipitation and polymorphism. Biofilms contain abundant EPS, which influence $CaCO_3$ precipitation principally due the presence of negatively charged, Ca^{2+}-binding organic functional groups (Dupraz *et al.*, 2009), and have been shown exert a control on $CaCO_3$ polymorphism in laboratory experiments (Tourney & Ngwenya, 2008, 2009). Microlaminations formed by alternating layers of aragonite and calcite in hot spring travertines in Japan were interpreted as resulting from diurnal cycles affecting microbial EPS (Okumura *et al.*, 2013b): during the day, EPS built by photosynthetic organisms would bind Ca^{2+}, reducing supersaturation and promoting calcite formation, while at night, decomposition of EPS by heterotrophs would release Ca^{2+} and lead to aragonite precipitation. Similarly, $CaCO_3$ polymorphism in Italian hot spring travertine deposits was interpreted to reflect microbial diurnal control (Guo & Riding, 1992), but there aragonite was thought to grow during the day. Different types of microbial metabolisms, including oxygenic photosynthesis (performed by cyanobacteria and microalgae visibly thriving at the surface of Crystal Geyser travertines in warm months; Fig. S1A,B) may cause local increases in alkalinity and saturation with respect to $CaCO_3$ phases (Dupraz *et al.*, 2009), also possibly affecting $CaCO_3$ polymorphism. $CaCO_3$ polymorphism in microbial precipitation experiments was recently shown to be affected by bacterial metabolism in a strain-specific way, which was interpreted as differential precipitation kinetics resulting from different levels of enzymatic activities (Clarà Saracho *et al.*, 2020). It can be concluded that different types of microbial processes may be responsible for the small-scale variations in $CaCO_3$ polymorphism in Crystal Geyser travertines, but that, as opposed to the pisoids, iron redox dynamics is not an important factor. Barth & Chafetz (2015) reported the presence of iron-rich tube-like structures morphologically similar to the iron sheaths produced by microaerophilic iron-oxidizing bacteria such as *Leptothrix ochracea* (Fleming *et al.*, 2011) in Crystal Geyser's travertines. However, the absence of well-defined ferrihydrite layers suggests that the travertine-formation area does not experience intense blooms of iron oxidizers. Moreover, iron oxidizers were not detected in bacterial 16s rDNA phylotype analyses performed on a Crystal Geyser travertine sample by Takashima *et al.* (2011), showing that they are not dominant members of the bacterial community thriving at the surface of these travertines.

CONCLUSIONS

Pisoids and travertines formed at Crystal Geyser, a natural analogue for CO_2 leakage at CCS sites, were characterized. Microbially driven iron oxidation was shown to exert a strong influence on $CaCO_3$ polymorphism, as recorded in the pisoids. In the travertines, microbial activity may produce small-scale variations in $CaCO_3$ polymorphism, and textural features such as laminations and calcified gas bubbles. A control on $CaCO_3$ polymorphism by iron redox dynamics was shown here for the first time in a natural environment. Microbial iron oxidation may play an important role in controlling polymorphism of the carbonate products of CO_2 escape from geological storage, and may also be relevant to subsurface carbonation at CCS sites. Indeed, blooms of iron-oxidizing Betaproteobacteria have been occurring following CO_2 injections at a geological CO_2 storage site (Trias *et al.*, 2017). Fractures can introduce oxygen in deep groundwater, creating iron-oxidizer hotspots in the subsurface (Bochet *et al.*, 2020). Future studies will have to determine whether intense microbial iron oxidation may influence subsurface carbonate formation and stability, impacting the efficacy of geological CO_2 storage.

ACKNOWLEDGMENTS

This research was supported by funding from the NASA Astrobiology Institute to the Rock Powered Life Team (NNA15BB02A). The authors thank Joanne Emerson (University of California, Davis) for introducing us to the Crystal Geyser field site. Fred Luiszer is thanked for his assistance with geochemical measurements, which were conducted at the Laboratory for Environmental and Geological Studies (University of Colorado (Boulder, CO). SEM was performed at the Nanoscale Fabrication Laboratory at the University of Colorado (Boulder, CO). Raman analyses were conducted at the Raman Microspectroscopy Laboratory at the Department of Geological Sciences, University of Colorado (Boulder, CO). STXM was performed at the

Canadian Light Source (Saskatoon, Saskatchewan, Canada), a national research facility of the University of Saskatchewan, which is supported by the Canada Foundation for Innovation (CFI), the Natural Sciences and Engineering Research Council (NSERC), the National Research Council (NRC), the Canadian Institutes of Health Research (CIHR), the Government of Saskatchewan, and the University of Saskatchewan. Jian Wang is thanked for providing support on STXM beamline SM at the Canadian Light Source. S K-edge XANES analyses were performed at the Stanford Synchrotron Radiation Lightsource (Stanford, CA, USA). Use of the Stanford Synchrotron Radiation Lightsource, SLAC National Accelerator Laboratory, is supported by the U.S. Department of Energy, Office of Science, Office of Basic Energy Sciences under Contract No. DE-AC02-76SF00515. Roger Everett Summons is thanked for his assistance and the use of his laboratory facilities at Massachusetts Institute of Technology. The Irish Research Council and the Marie Sklodowska-Curie Actions programme are acknowledged for funding support for SOR (ELEVATE programme, grant ID: 291760).

DATA AVAILABILITY STATEMENT

The data supporting the findings of this study are openly available in the supplied supplementary figures and tables.

TABLE

SiO_2 and cations	Si ppm	Mn ppm	Fe ppm	Mg ppm	Ca ppm	Al ppm	Sr ppm	Na ppm	K ppm
Detection limit	*0.026*	*0.001*	*0.003*	*0.002*	*0.003*	*0.002*	*0.001*	*0.020*	*0.029*
2014-1	8.12	1.86	10.61	249.6	1089	<DL	15.4	4231.5	351.9
2014-2	8.14	1.84	10.56	248.2	1092	<DL	15.3	4303.9	370.2
2015	6.6	1.37	6.14	221.3	955	<DL		3616	324

Anions	F ppm	Cl ppm	NO_2 ppm	Br ppm	NO_3 ppm	PO_4 ppm	SO_4 ppm
Detection limit	*0.02*	*0.02*	*0.03*	*0.05*	*0.05*	*0.2*	*0.2*
2014-1	<DL	4817	<DL	1.29	<DL	<DL	2433.9
2014-2	<DL	4830	<DL	1.38	<DL	<DL	2432.4

Table 1. Major elements in Crystal Geyser vent waters collected in April 2014 (on two different days) and in February 2015. <DL: below detection limit. Note that Sr and anions were not measured in 2015.

FIGURES

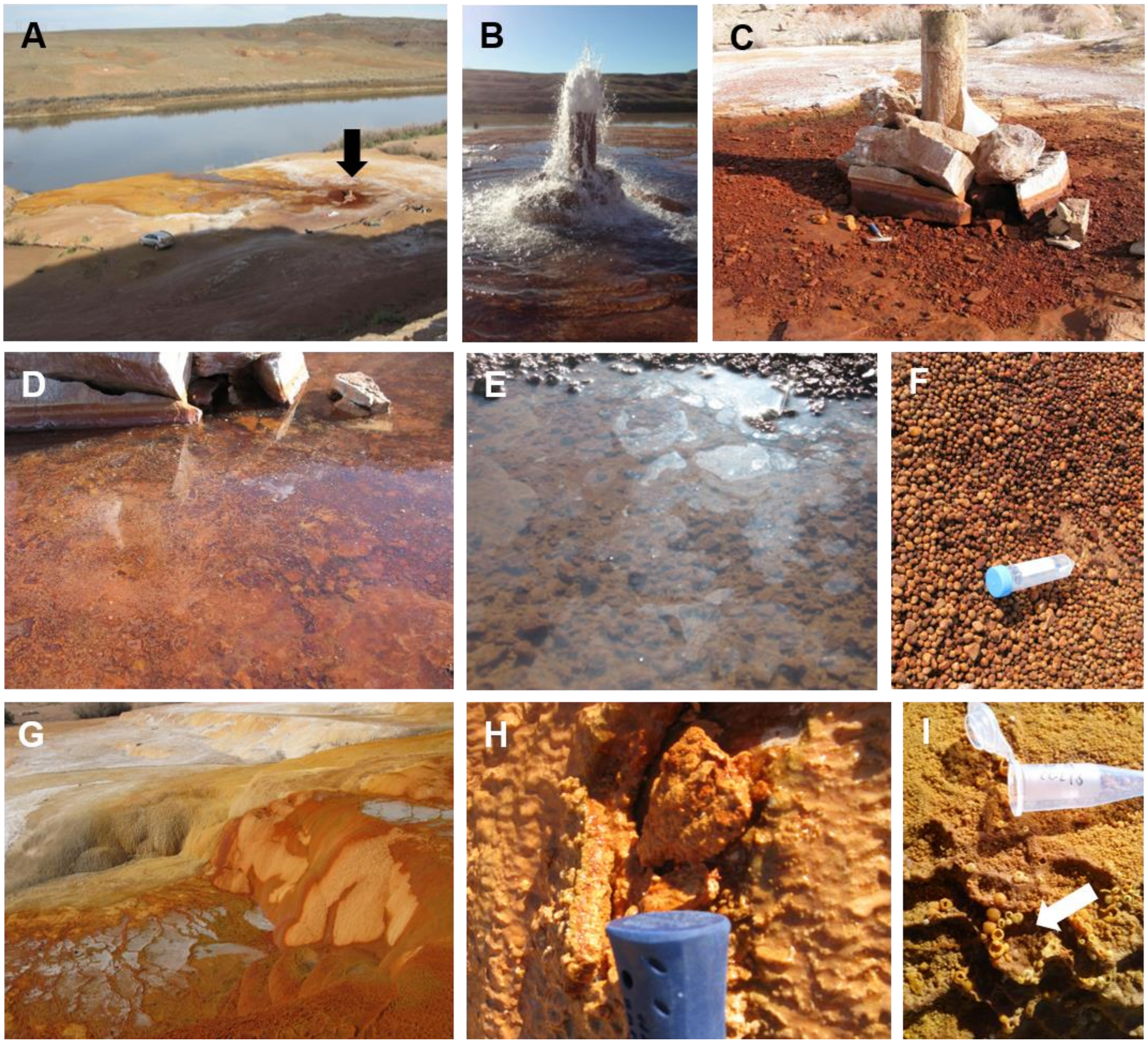

Figure 1. Photographs of the Crystal Geyser field site, pools, pisoids and travertines. (A) Aerial view of Crystal Geyser (black arrow) between two eruptions. The reddish pool around the geyser is visible, as well as the orange travertines deposited downstream along the flow path of the geyser waters to Green River. (B) Crystal Geyser during an eruption. (C) The geyser and its surrounding pools completely dry up between eruptions. (D) Pool formed around the geyser after

an eruption. Iron-(oxyhydr)oxides forming at the surface of the pool are visible. (E) Oily-looking films formed at the surface of wet pools in the pisoid-formation area. (F) Pisoids found near the geyser. 50 mL falcon tube shown for scale. (G) Terraced travertines found downstream. (H) Close-up on a section of the “layered” travertine (TL). Rock hammer grip shown for scale. (I) Calcified bubbles (white arrow) at the surface of the “bubbly” travertine (TB). 1.5 mL microcentrifuge tube shown for scale. Photographs were taken in April 2014 (A, C-H) and February 2015 (B,I).

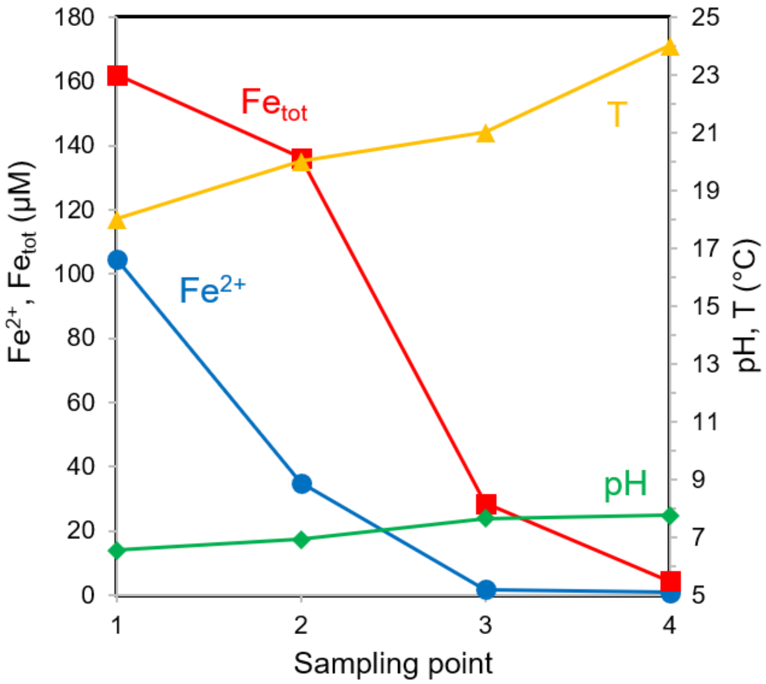

Figure 2. Geochemical profiles along the flow path of Crystal Geyser waters. Sampling point #1 corresponds to the pool directly surrounding the geyser, and sampling point #4 corresponds to the water entering Green River. Blue circles: concentration of dissolved Fe(II) (Fe^{2+}). Red squares: concentration of total dissolved Fe (Fe_{tot}). Yellow triangles: temperature (T). Green diamonds: pH.

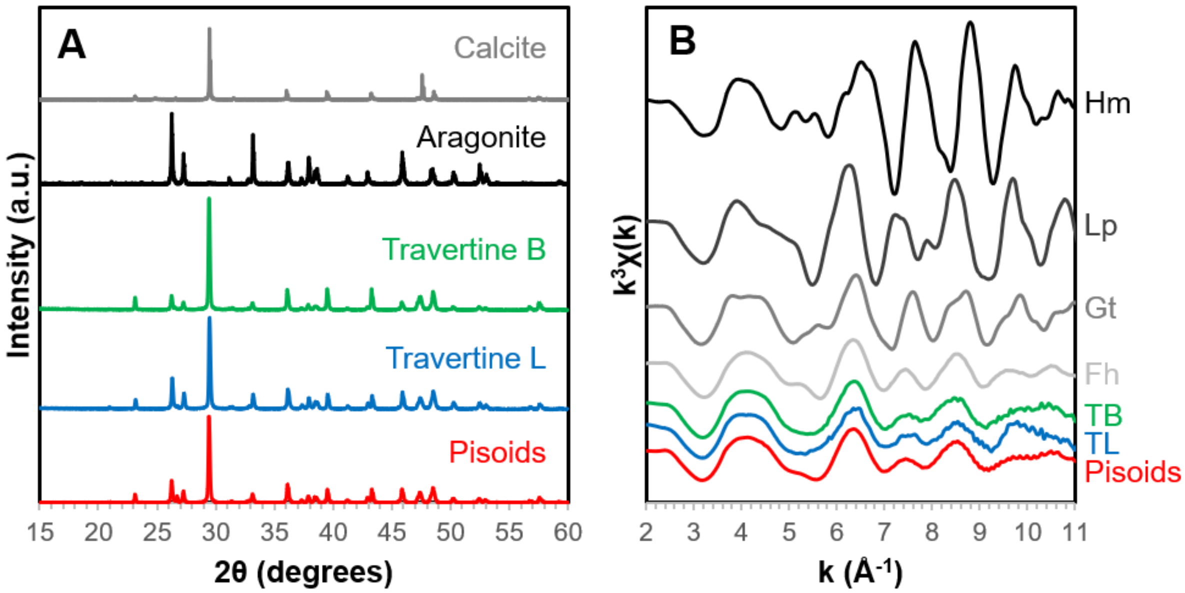

Figure 3. Mineralogy of the Crystal Geyser travertines (TL and TB) and pisoids. (A) XRD spectra. (B) Fe K-edge EXAFS spectra. Reference spectra for calcite and aragonite (A) and ferrihydrite (Fh), Goethite (Gt), Lepidocrocite (Lp) and Hematite (Hm) (B) shown for comparison.

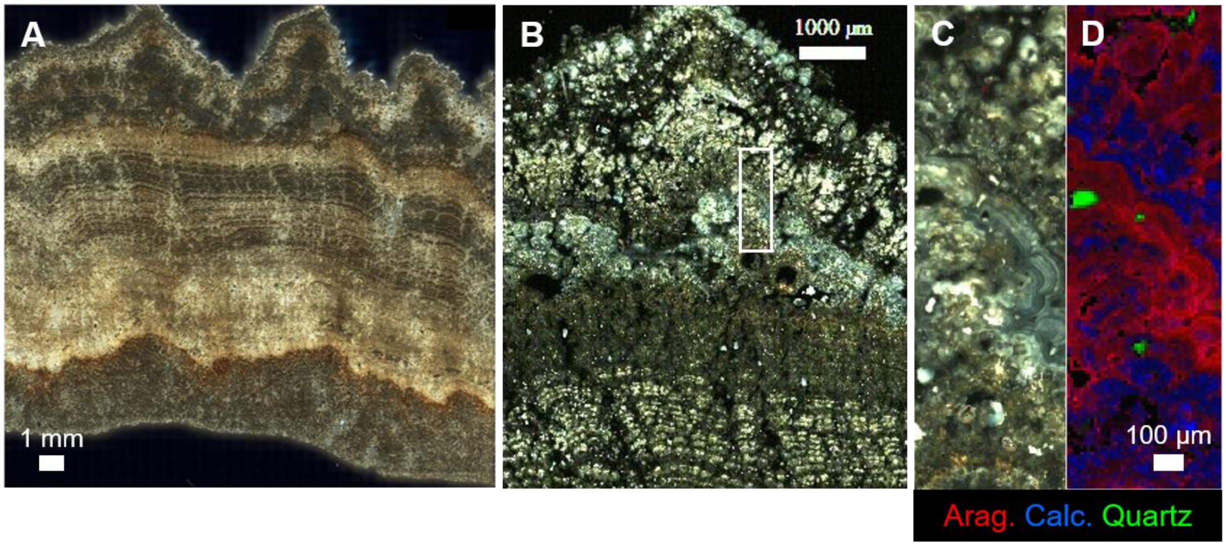

Figure 4. Micrographs and Raman map of the “layered” travertine (TB). (A) Large composite micrograph in cross-polarized transmitted light. (B) Close-up in cross-polarized light showing the location of the Raman map (white rectangle). (C) Cross-polarized image corresponding to the area mapped with Raman. (D) Raman map showing the distribution of aragonite (red), calcite (blue) and quartz (green).

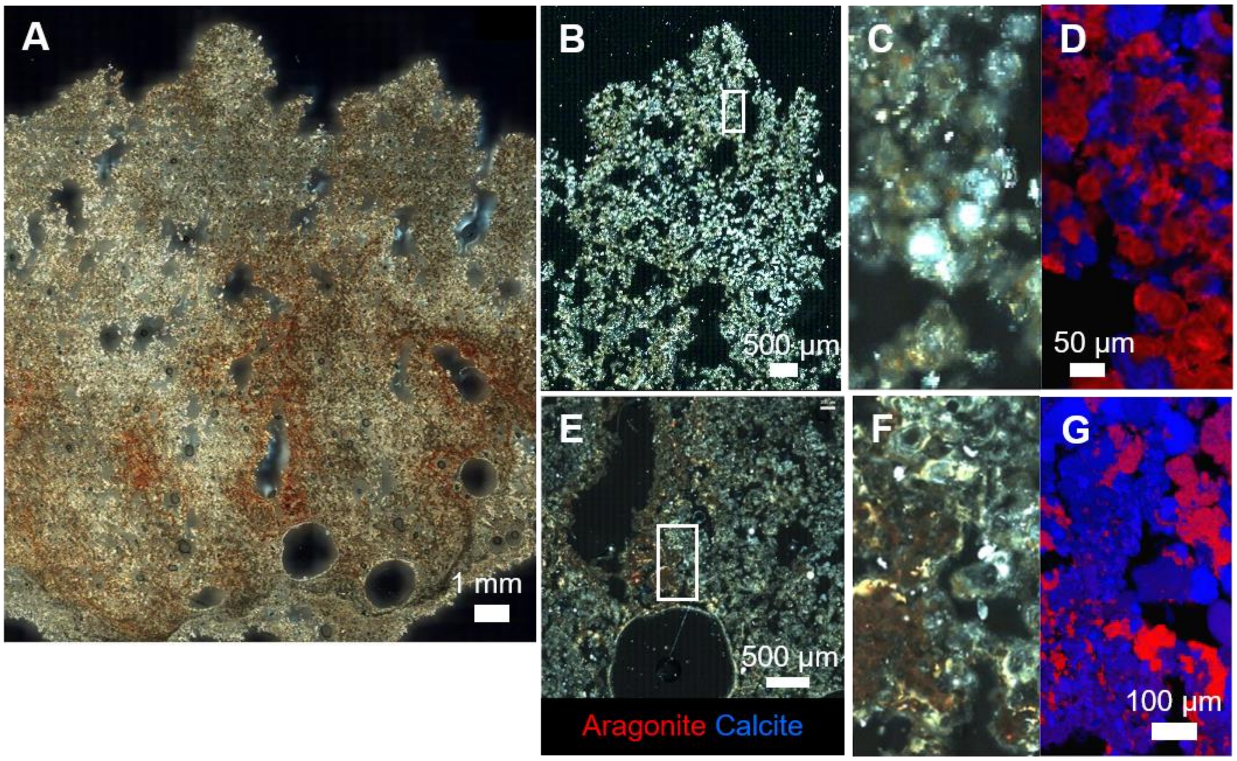

Figure 5. Micrographs and Raman maps of the “bubbly” travertine (TB). (A) Large composite micrograph in cross-polarized transmitted light. (B,E) Close-ups in cross-polarized light showing the location of the Raman maps (white rectangles). (C,F) Cross-polarized images corresponding to the areas mapped with Raman. (D,G) Raman maps showing the distribution of aragonite (red) and calcite (blue).

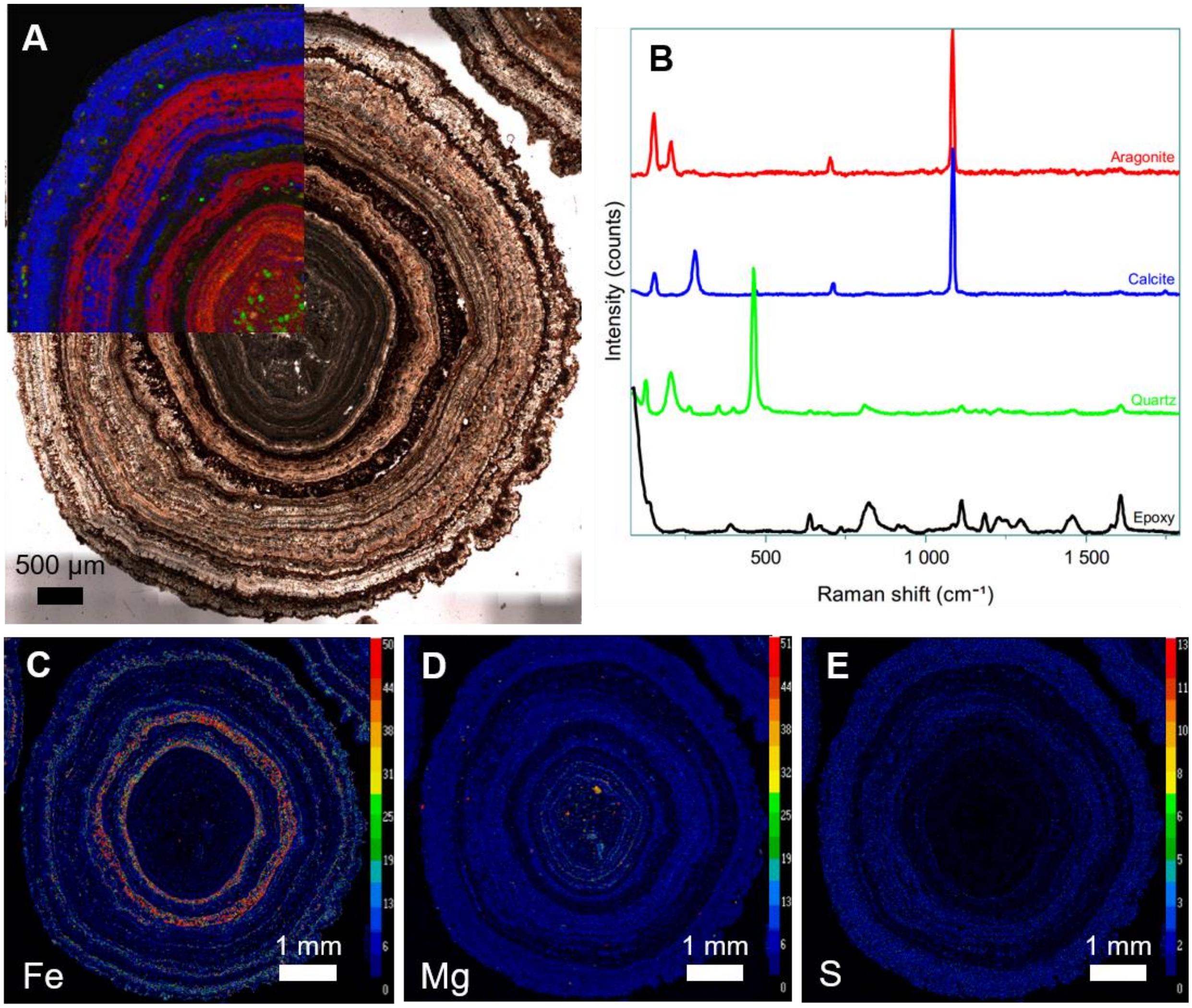

Figure 6. Mineralogical and chemical mapping of a simple pisoid. (A) Montage of transmitted light micrographs and overlaid Raman map of a pisoid, showing the distribution of aragonite (red) and calcite (blue), as well as quartz (green). (B) Representative end-member Raman spectra of aragonite, calcite, quartz, and embedding epoxy resin, used to fit the map datasets. (C-E) Elemental maps of Fe, Mg and S acquired on the same pisoid using EPMA. The color scales represent relative abundances of the different elements in the sample, but the number indicated on the scales are arbitrary (no calibration has been performed).

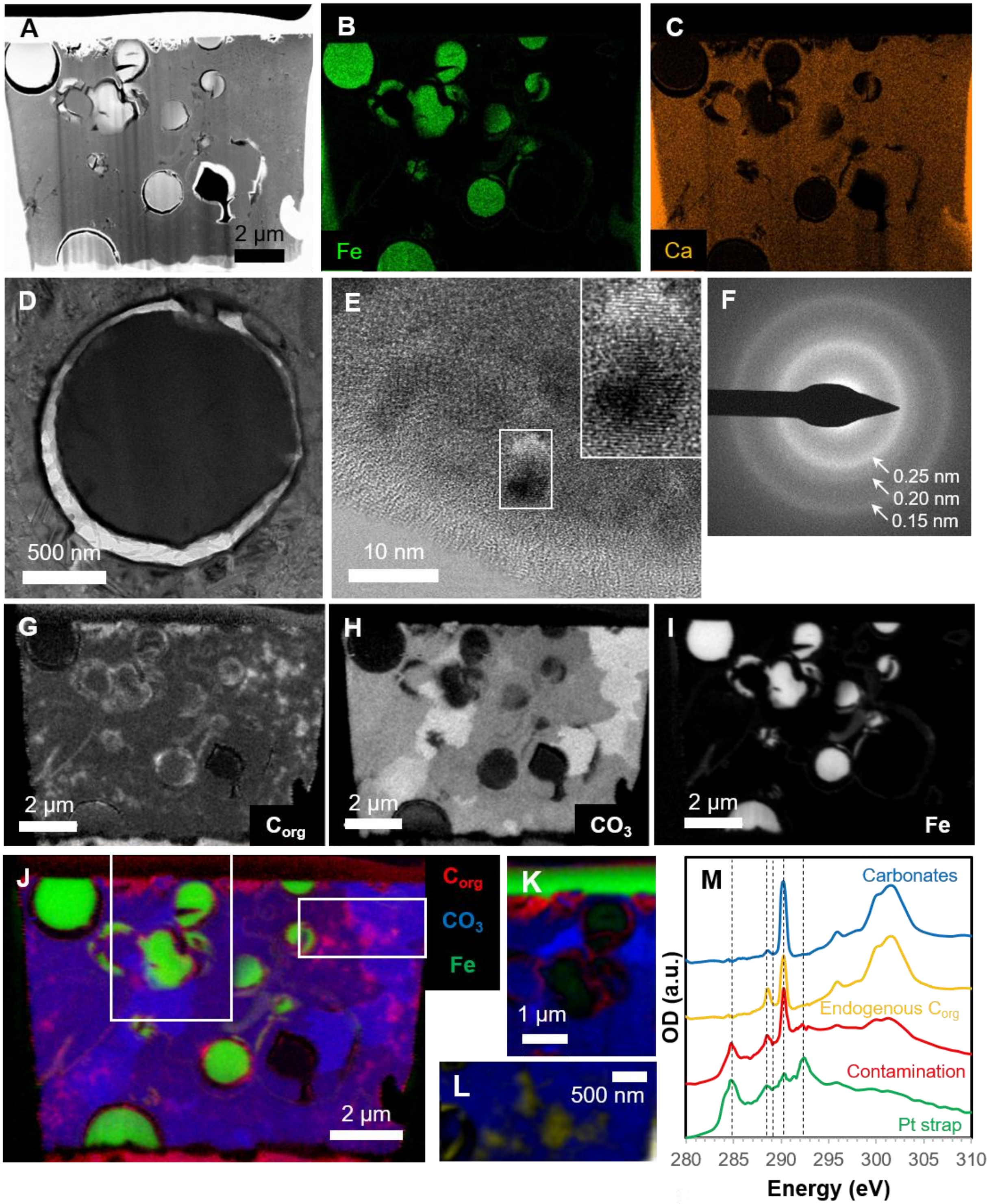
A
2 µm
B
Fe
C
Ca
D
500 nm
E
10 nm
F
0.25 nm
0.20 nm
0.15 nm
G
2 µm
C_{org}
H
2 µm
CO_3
I
2 µm
Fe
J
2 µm
C_{org}
CO_3
Fe
K
1 µm
L
500 nm
M
Carbonates
Endogenous C_{org}
Contamination
Pt strap
OD (a.u.)
280
285
290
295
300
305
310
Energy (eV)

Figure 7. TEM (A-F) and STXM (G-M) analyses of FIB section 1 (pisoid). (A) STEM high angle annular dark field image. (B) Fe map. (C) Ca map. (D) Bright field TEM close-up on an iron-rich spherule. (E) High-resolution TEM image obtained on the border of a spherule. Small (<10 nm) crystalline domains are visible. A close-up on a crystalline domain shows lattice fringes with a spacing of ~0.2 nm. (F) SAED pattern obtained on the spherule border, showing diffuse rings, and confirming the nanocrystalline structure of the spherules. d-spacing values, corresponding to ferrihydrite, are indicated. (G) Organic carbon map. (H) Carbonate maps. (I) Iron map. (J) Composite STXM map showing the distribution of organic carbon (red), carbonates (blue) and iron (green). The white boxes show the areas corresponding to maps and spectra shown in (K-M). (K) Map showing the protective platinum layer at the top of the FIB section 1 (green), contaminating organics (red) and carbonate minerals (blue). (L) Map showing organic-rich areas (yellow) and carbonate minerals (blue). (M) Representative C K-edge XANES spectra for the carbonate matrix, the platinum layer, and organic contaminants in (K) and the organic-rich areas in (L). Vertical lines show the positions of absorption peaks at 284.9 eV, 286.1 eV, 287.4 eV, 288.6 eV, 290.3 eV and 292.4 eV.

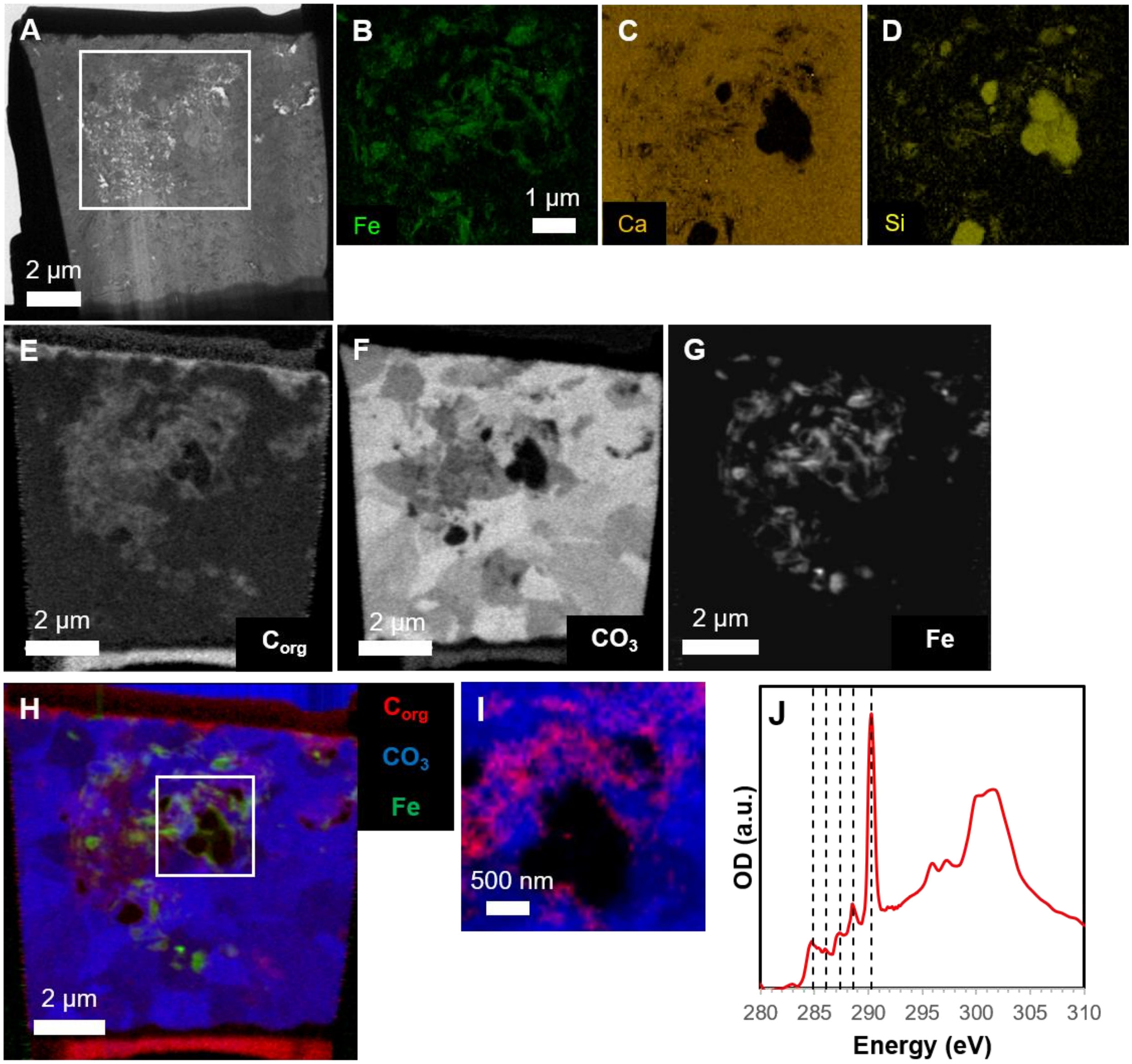

Figure 8. TEM (A-D) and STXM (E-J) analyses of FIB section 2 (pisoid). (A) TEM bright field image of the whole section. The white rectangle shows the areas mapped in (B-D). (B) Fe map. (C) Ca map. (D) Si map showing the presence of quartz grains. (E) Organic carbon map. (F) Carbonate map. (G) Iron map. (H) Composite STXM map showing the distribution of organic carbon (red), carbonates (blue) and iron (green). The white box shows the areas mapped in (I).

(I) Map showing the distribution of organic matter (red) and carbonate minerals (blue). (J) C K-edge XANES spectrum representative of the organic matter mapped in red in (I). Vertical lines show the positions of absorption peaks at 284.9 eV, 286.1 eV, 287.4 eV, 288.6 eV, and 290.3 eV.

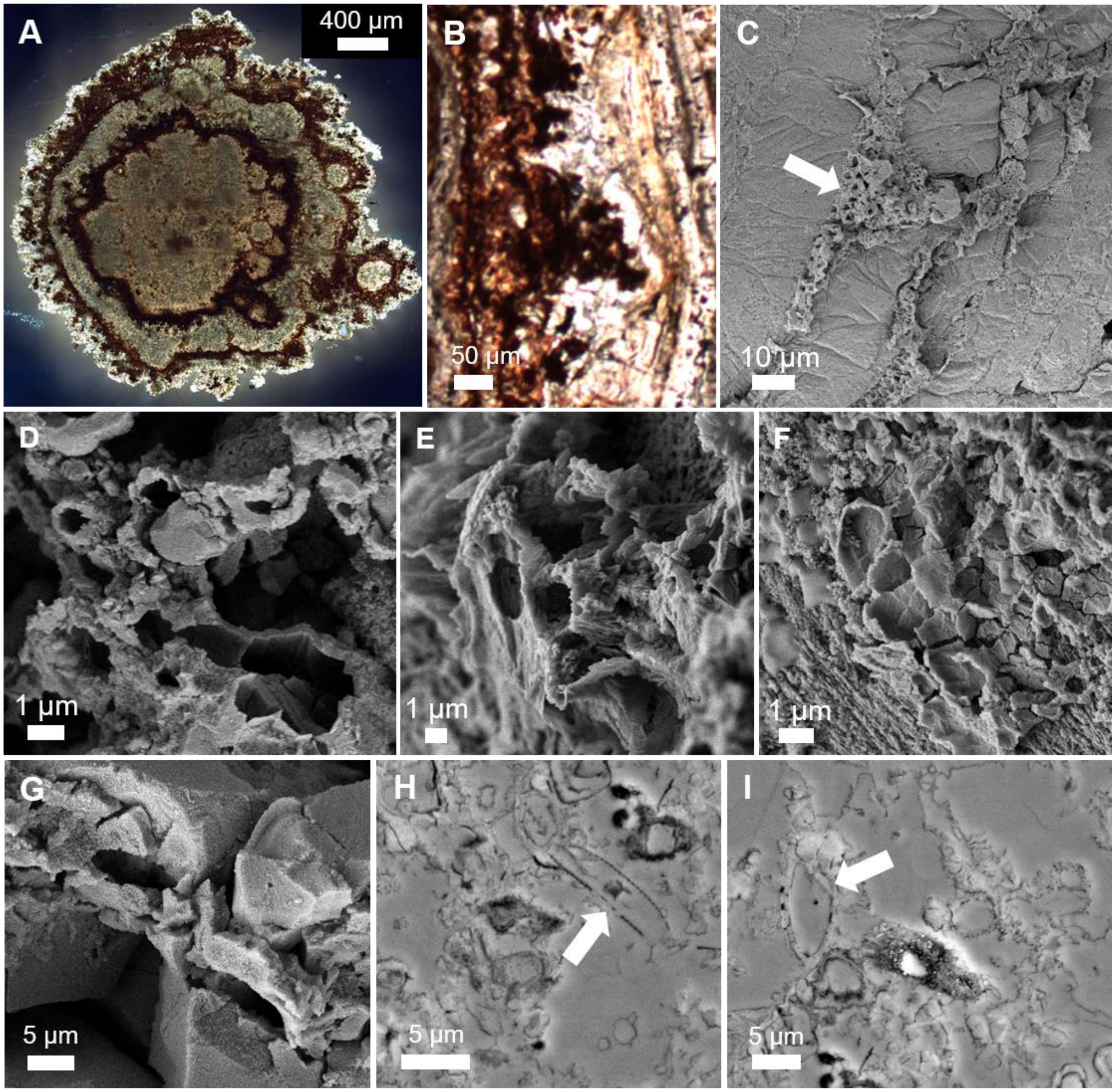

Figure 9. Optical micrographs and SEM of pisoids. (A) Montage of light micrographs showing a pisoid. (B) Close-up on iron shrubs. (C-F) SEM images of HCl-etched pisoids. (C) Low magnification image showing the partially dissolved carbonate matrix revealing the structure of an Fe-rich layer (arrow). (D-F) Close-ups showing microbial iron casts. The images were obtained on three different pisoids. (G-I) SEM images of microbial shapes in carbonate layers of

the pisoids. (G) Empty rod-shaped casts. (H,I) Possible microalgae entombed in the carbonates (arrows). (G) was acquired on a HCl-etched sample. (H,I) were acquired on a polished thin section.

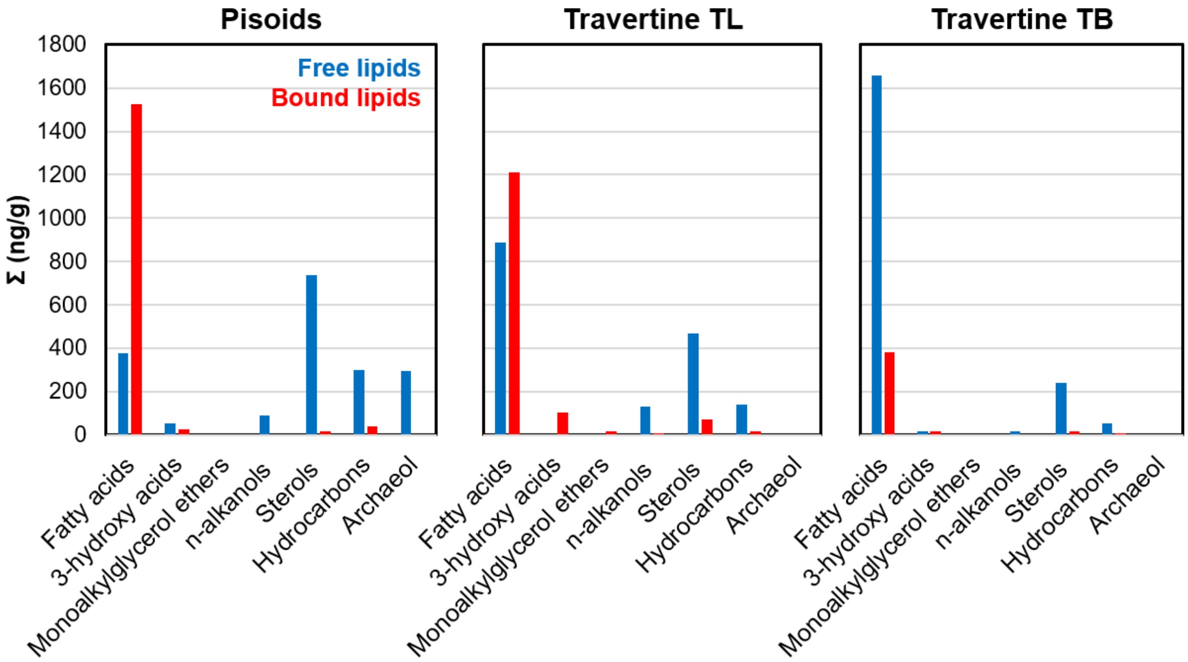

867

868 **Figure 10.** Free and carbonate-bound lipid components in Crystal Geyser pisoids and travertines

869 (TL and TB).

870

871

REFERENCES

Alcalde, J., **Flude, S.**, **Wilkinson, M.**, **Johnson, G.**, **Edlmann, K.**, **Bond, C.E.**, **Scott, V.**, **Gilfillan, S.M.V.**, **Ogaya, X.** and **Haszeldine, R.S.** (2018) Estimating geological CO2 storage security to deliver on climate mitigation. *Nat Commun*, **9**, 2201.

Assayag, N., **Bickle, M.**, **Kampman, N.** and **Becker, J.** (2009) Carbon isotopic constraints on CO2 degassing in cold-water Geysers, Green River, Utah. *Energy Procedia*, **1**, 2361–2366.

Baer, J.L. and **Rigby, J.K.** (1978) Geology of the Crystal Geyser and environmental implications of its effluent, Grand County, Utah, Utah Geology. *Utah Geology*, **5**, 125–130.

Barth, J.A. and **Chafetz, H.S.** (2015) Cool water geyser travertine: Crystal Geyser, Utah, USA. *Sedimentology*, **62**, 607–620.

Blackwell, N., **Perkins, W.**, **Palumbo-Roe, B.**, **Bearcock, J.**, **Lloyd, J.R.** and **Edwards, A.** (2019) Seasonal blooms of neutrophilic Betaproteobacterial Fe(II) oxidizers and Chlorobi in iron-rich coal mine drainage sediments. FEMS Microbiology Ecology. doi: 10.1093/femsec/fiz140

Bochet, O., **Bethencourt, L.**, **Dufresne, A.**, **Farasin, J.**, **Pédrot, M.**, **Labasque, T.**, **Chatton, E.**, **Lavenant, N.**, **Petton, C.**, **Abbott, B.W.**, **Aquilina, L.** and **Le Borgne, T.** (2020) Iron-oxidizer hotspots formed by intermittent oxic–anoxic fluid mixing in fractured rocks. *Nature Geoscience*, **13**, 149–155.

Bosak, T., **Bush, J.W.M.**, **Flynn, M.R.**, **Liang, B.**, **Ono, S.**, **Petroff, A.P.** and **Sim, M.S.** (2010) Formation and stability of oxygen-rich bubbles that shape photosynthetic mats: Formation and stability of oxygen-rich bubbles. *Geobiology*, **8**, 45–55.

Brandes, J.A., **Lee, C.**, **Wakeham, S.**, **Peterson, M.**, **Jacobsen, C.**, **Wirick, S.** and **Cody, G.** (2004) Examining marine particulate organic matter at sub-micron scales using scanning transmission X-ray microscopy and carbon X-ray absorption near edge structure spectroscopy. *Marine Chemistry*, **92**, 107–121.

Brandes, J.A., **Wirick, S.** and **Jacobsen, C.** (2010) Carbon K-edge spectra of carbonate minerals. *Journal of Synchrotron Radiation*, **17**, 676–682.

Burnside, N.M., **Shipton, Z.K.**, **Dockrill, B.** and **Ellam, R.M.** (2013) Man-made versus natural CO2 leakage: A 400 k.y. history of an analogue for engineered geological storage of CO2. *Geology*, **41**, 471–474.

Carlut, J., **Benzerara, K.**, **Horen, H.**, **Menguy, N.**, **Janots, D.**, **Findling, N.**, **Addad, A.** and **Machouk, I.** (2010) Microscopy study of biologically mediated alteration of natural midoceanic ridge basalts and magnetic implications. Journal of Geophysical Research. doi: 10.1029/2009JG001139

Chafetz, H., **Barth, J.**, **Cook, M.**, **Guo, X.** and **Zhou, J.** (2018) Origins of carbonate spherulites: Implications for Brazilian Aptian pre-salt reservoir. *Sedimentary Geology*, **365**, 21–33.

Chafetz, H.S., **Akdim, B.**, **Julia, R.** and **Reid, A.** (1998) Mn- and Fe-rich black travertine shrubs; bacterially (and nanobacterially) induced precipitates. *Journal of Sedimentary Research*, **68**, 404–412.

Chafetz, H.S. and **Guidry, S.A.** (1999) Bacterial shrubs, crystal shrubs, and ray-crystal shrubs: bacterial vs. abiotic precipitation. *Sedimentary Geology*, **126**, 57–74.

Chan, C.S., **Fakra, S.C.**, **Emerson, D.**, **Fleming, E.J.** and **Edwards, K.J.** (2011) Lithotrophic iron-oxidizing bacteria produce organic stalks to control mineral growth: implications for biosignature formation. *The ISME Journal*, **5**, 717–727.

Chan, C.S., **McAllister, S.M.**, **Leavitt, A.H.**, **Glazer, B.T.**, **Krepski, S.T.** and **Emerson, D.** (2016) The Architecture of Iron Microbial Mats Reflects the Adaptation of Chemolithotrophic Iron Oxidation in Freshwater and Marine Environments. Front Microbiol. doi: 10.3389/fmicb.2016.00796

Chang, R., **Kim, S.**, **Lee, S.**, **Choi, S.**, **Kim, M.** and **Park, Y.** (2017) Calcium Carbonate Precipitation for CO2 Storage and Utilization: A Review of the Carbonate Crystallization and Polymorphism. Front Energy Res. doi: 10.3389/fenrg.2017.00017

Clarà Saracho, A., **Haigh, S.K.**, **Hata, T.**, **Soga, K.**, **Farsang, S.**, **Redfern, S.A.T.** and **Marek, E.** (2020) Characterisation of CaCO 3 phases during strain-specific ureolytic precipitation. *Scientific Reports*, **10**, 10168.

Cosmidis, J. and **Benzerara, K.** (2014) Soft X-ray Scanning Transmission Spectromicroscopy. In: *Biomineralization Sourcebook: Characterization of Biominerals and Biomimetic Materials*, CRC Press, *E. DiMasi and L.B. Gower*, London, UK, 115–133.

Cosmidis, J., **Benzerara, K.**, **Menguy, N.** and **Arning, E.** (2013) Microscopy evidence of bacterial microfossils in phosphorite crusts of the Peruvian shelf: Implications for phosphogenesis mechanisms. *Chemical Geology*, **359**, 10–22.

de Leeuw, N.H. (2002) Molecular Dynamics Simulations of the Growth Inhibiting Effect of Fe2+, Mg2+ , Cd2+ , and Sr2+ on Calcite Crystal Growth. *J. Phys. Chem. B*, **106**, 5241–5249.

Della Porta, G., **Hoppert, M.**, **Hallmann, C.**, **Schneider, D.** and **Reitner, J.** (2021) The influence of microbial mats on travertine precipitation in active hydrothermal systems (Central Italy). The Depositional Record. doi: https://doi.org/10.1002/dep2.147

Diaz, M.R., **Eberli, G.P.**, **Blackwelder, P.**, **Phillips, B.** and **Swart, P.K.** (2017) Microbially mediated organomineralization in the formation of ooids. *Geology*, **45**, 771–774.

Diaz, M.R., **Swart, P.K.**, **Eberli, G.P.**, **Oehlert, A.M.**, **Devlin, Q.**, **Saeid, A.** and **Altabet, M.A.** (2015) Geochemical evidence of microbial activity within ooids. *Sedimentology*, **62**, 2090–2112.

Dupraz, C., **Reid, R.P.**, **Braissant, O.**, **Decho, A.W.**, **Norman, R.S.** and **Visscher, P.T.** (2009) Processes of carbonate precipitation in modern microbial mats. *Earth-Science Reviews*, **96**, 141–162.

Dyer, B.D. (2003) A field guide to bacteria. *Cornell University Press*, Ithaca, N.Y, 355 pp.

Emerson, D. and **Moyer, C.** (1997) Isolation and characterization of novel iron-oxidizing bacteria that grow at circumneutral pH. *Appl. Environ. Microbiol.*, **63**, 4784–4792.

Emerson, J.B., **Thomas, B.C.**, **Alvarez, W.** and **Banfield, J.F.** (2016) Metagenomic analysis of a high carbon dioxide subsurface microbial community populated by chemolithoautotrophs and bacteria and archaea from candidate phyla: High CO_2 subsurface metagenomics. *Environmental Microbiology*, **18**, 1686–1703.

Fleming, E.J., **Cetinić, I.**, **Chan, C.S.**, **Whitney King, D.** and **Emerson, D.** (2014) Ecological succession among iron-oxidizing bacteria. *The ISME Journal*, **8**, 804–815.

Fleming, E.J., **Langdon, A.E.**, **Martinez-Garcia, M.**, **Stepanauskas, R.**, **Poulton, N.J.**, **Masland, E.D.P.** and **Emerson, D.** (2011) What's new is old: resolving the identity of Leptothrix ochracea using single cell genomics, pyrosequencing and FISH. *PLoS One*, **6**, e17769.

Fru, E.C., **Piccinelli, P.** and **Fortin, D.** (2012) Insights into the Global Microbial Community Structure Associated with Iron Oxyhydroxide Minerals Deposited in the Aerobic Biogeosphere. *Geomicrobiology Journal*, **29**, 587–610.

Gilfillan, S.M.V., **Ballentine, C.J.**, **Holland, G.**, **Blagburn, D.**, **Lollar, B.S.**, **Stevens, S.**, **Schoell, M.** and **Cassidy, M.** (2008) The noble gas geochemistry of natural CO2 gas reservoirs from the Colorado Plateau and Rocky Mountain provinces, USA. *Geochimica et Cosmochimica Acta*, **72**, 1174–1198.

González, A.G., **Pokrovsky, O.S.**, **Jiménez-Villacorta, F.**, **Shirokova, L.S.**, **Santana-Casiano, J.M.**, **González-Dávila, M.** and **Emnova, E.E.** (2014) Iron adsorption onto soil and aquatic bacteria: XAS structural study. *Chemical Geology*, **372**, 32–45.

Gouveia, F.J. and **Friedmann, S.J.** (2006) Timing and prediction of CO2 eruptions from Crystal Geyser, UT. *United States Department of Energy*.

Gouveia, F.J., **Johnson, M.R.**, **Leif, R.N.** and **Friedmann, S.J.** (2005) Aerometric measurement and modeling of the mass of CO2 emissions from Crystal Geyser, Utah. *Lawrence Livermore National Lab., Livermore, CA (US)*.

Grădinaru, M., **Lazăr, I.**, **Ducea, M.N.** and **Petrescu, L.** (2020) Microaerophilic Fe-oxidizing micro-organisms in Middle Jurassic ferruginous stromatolites and the paleoenvironmental context of their formation (Southern Carpathians, Romania). *Geobiology*, **18**, 366–393.

Guido, A., **Rosso, A.**, **Sanfilippo, R.**, **Russo, F.** and **Mastandrea, A.** (2016) Frutexites from microbial/metazoan bioconstructions of recent and Pleistocene marine caves (Sicily, Italy). *Palaeogeography, Palaeoclimatology, Palaeoecology*, **453**, 127–138.

Guo, L. and **Riding, R.** (1992) Aragonite laminae in hot water travertine crusts, Rapolano Terme, Italy. *Sedimentology*, **39**, 1067–1079.

Gutjahr, A., **Dabringhaus, H.** and **Lacmann, R.** (1996) Studies of the growth and dissolution kinetics of the CaCO3 polymorphs calcite and aragonite II. The influence of divalent cation additives on the growth and dissolution rates. *Journal of Crystal Growth*, **158**, 310–315.

Han, W.S., **Lu, M.**, **McPherson, B.J.**, **Keating, E.H.**, **Moore, J.**, **Park, E.**, **Watson, Z.T.** and **Jung, N.-H.** (2013) Characteristics of CO2-driven cold-water geyser, Crystal Geyser in Utah: experimental observation and mechanism analyses. *Geofluids*, **13**, 283–297.

Han, W.S., **Watson, Z.T.**, **Kampman, N.**, **Grundl, T.**, **Graham, J.P.** and **Keating, E.H.** (2017) Periodic changes in effluent chemistry at cold-water geyser: Crystal geyser in Utah. *Journal of Hydrology*, **550**, 54–64.

Heath, J.E., **Lachmar, T.E.**, **Evans, J.P.**, **Kolesar, P.T.** and **Williams, A.P.** (2009) Hydrogeochemical Characterization of Leaking, Carbon Dioxide-Charged Fault Zones in East-Central Utah, With Implications for Geologic Carbon Storage. In: *Carbon Sequestration and Its Role in the Global Carbon Cycle*, *American Geophysical Union (AGU)*, 147–158.

Hitchcock, A. (2012) aXis 2000 - Analysis of X-ray Images and Spectra. http://unicorn.mcmaster.ca/aXis2000.html. Accessed 16 Feb 2012

Holland, H.D., **Kirsipu, T.V.**, **Huebner, J.S.** and **Oxburgh, U.M.** (1964) On Some Aspects of the Chemical Evolution of Cave Waters. *The Journal of Geology*, **72**, 36–67.

Ilina, S.M., **Lapitskiy, S.A.**, **Alekhin, Y.V.**, **Viers, J.**, **Benedetti, M.** and **Pokrovsky, O.S.** (2016) Speciation, Size Fractionation and Transport of Trace Elements in the Continuum

Soil Water–Mire–Humic Lake–River–Large Oligotrophic Lake of a Subarctic Watershed. *Aquat Geochem*, **22**, 65–95.

Jakubowicz, M., **Belka, Z.** and **Berkowski, B.** (2014) Frutexites encrustations on rugose corals (Middle Devonian, southern Morocco): complex growth of microbial microstromatolites. *Facies*, **60**, 631–650.

Jones, B. (2017) Review of calcium carbonate polymorph precipitation in spring systems. *Sedimentary Geology*, **353**, 64–75.

Kampman, N., **Bickle, M.J.**, **Maskell, A.**, **Chapman, H.J.**, **Evans, J.P.**, **Purser, G.**, **Zhou, Z.**, **Schaller, M.F.**, **Gattacceca, J.C.**, **Bertier, P.**, **Chen, F.**, **Turchyn, A.V.**, **Assayag, N.**, **Rochelle, C.**, **Ballentine, C.J.** and **Busch, A.** (2014) Drilling and sampling a natural CO2 reservoir: Implications for fluid flow and CO2-fluid–rock reactions during CO2 migration through the overburden. *Chemical Geology*, **369**, 51–82.

Kaneda, T. (1991) Iso- and anteiso-fatty acids in bacteria: biosynthesis, function, and taxonomic significance. *Microbiol Rev*, **55**, 288–302.

Kanellopoulos, C., **Thomas, C.**, **Xirokostas, N.** and **Ariztegui, D.** (2019) Banded Iron Travertines at the Ilia Hot Spring (Greece): An interplay of biotic and abiotic factors leading to a modern Banded Iron Formation analogue? *The Depositional Record*, **5**, 109–130.

Kano, A., **Okumura, T.**, **Takashima, C.** and **Shiraishi, F.** (2019) Sedimentology of Travertine. In: *Geomicrobiological Properties and Processes of Travertine*, *Springer Singapore*, Singapore, 43–66.

Kappler, A., **Bryce, C.**, **Mansor, M.**, **Lueder, U.**, **Byrne, J.M.** and **Swanner, E.D.** (2021) An evolving view on biogeochemical cycling of iron. *Nature Reviews Microbiology*, **19**, 360–374.

Kate, M. (1993) Chapter 9 Membrane lipids of archaea. In: *New Comprehensive Biochemistry* (Ed. M. Kates, D.J. Kushner, and A.T. Matheson), *Elsevier*, 26, 261–295.

Kaznatcheev, K.V., **Karunakaran, Ch.**, **Lanke, U.D.**, **Urquhart, S.G.**, **Obst, M.** and **Hitchcock, A.P.** (2007) Soft X-ray spectromicroscopy beamline at the CLS: Commissioning results. *Nuclear Instruments and Methods in Physics Research Section A: Accelerators, Spectrometers, Detectors and Associated Equipment*, **582**, 96–99.

Kelemen, P., **Benson, S.M.**, **Pilorgé, H.**, **Psarras, P.** and **Wilcox, J.** (2019) An Overview of the Status and Challenges of CO2 Storage in Minerals and Geological Formations. Front Clim. doi: 10.3389/fclim.2019.00009

Lehmann, J., **Solomon, D.**, **Brandes, J.**, **Fleckenstein, H.**, **Jacobson, C.** and **Thieme, J.** (2009) Synchrotron-Based Near-Edge X-Ray Spectroscopy of Natural Organic Matter in Soils and Sediments. In: *Biophysico-Chemical Processes Involving Natural Nonliving Organic Matter in Environmental Systems* (Ed. N. Senesi, B. Xing, and P.M. Huang), *John Wiley & Sons, Inc.*, Hoboken, NJ, USA, 729–781.

Lewicki, J.L., **Birkholzer, J.** and **Tsang, C.-F.** (2006) Natural and industrial analogues for leakage of CO2 from storage reservoirs: identification of features, events, and processes and lessons learned. *Environ Geol*, **52**, 457.

Liao, P., **Li, W.**, **Jiang, Y.**, **Wu, J.**, **Yuan, S.**, **Fortner, J.D.** and **Giammar, D.E.** (2017) Formation, Aggregation, and Deposition Dynamics of NOM-Iron Colloids at Anoxic–Oxic Interfaces. *Environ. Sci. Technol.*, **51**, 12235–12245.

Lin, Y.-P. and **Singer, P.C.** (2009) Effect of Mg2+ on the kinetics of calcite crystal growth. *Journal of Crystal Growth*, **312**, 136–140.

Maillot, F., **Morin, G.**, **Wang, Y.**, **Bonnin, D.**, **Ildefonse, P.**, **Chaneac, C.** and **Calas, G.** (2011) New insight into the structure of nanocrystalline ferrihydrite: EXAFS evidence for tetrahedrally coordinated iron(III). *Geochimica et Cosmochimica Acta*, **75**, 2708–2720.

Mejri, W., **Ben Salah, I.** and **Tlili, M.M.** (2015) Speciation of Fe(II) and Fe(III) effect on CaCO3 crystallization. *Crystal Research and Technology*, **50**, 236–243.

Mettler, S., **Wolthers, M.**, **Charlet, L.** and **Gunten, U. von** (2009) Sorption and catalytic oxidation of Fe(II) at the surface of calcite. *Geochimica et Cosmochimica Acta*, **73**, 1826–1840.

Meyer, H.J. (1984) The influence of impurities on the growth rate of calcite. *Journal of Crystal Growth*, **66**, 639–646.

Nielsen, M.R., **Sand, K.K.**, **Rodriguez-Blanco, J.D.**, **Bovet, N.**, **Generosi, J.**, **Dalby, K.N.** and **Stipp, S.L.S.** (2016) Inhibition of Calcite Growth: Combined Effects of Mg2+ and SO42–. *Crystal Growth & Design*, **16**, 6199–6207.

Okumura, T., **Takashima, C.** and **Kano, A.** (2013a) Textures and processes of laminated travertines formed by unicellular cyanobacteria in Myoken hot spring, southwestern Japan. *Island Arc*, **22**, 410–426.

Okumura, T., **Takashima, C.**, **Shiraishi, F.**, **Nishida, S.** and **Kano, A.** (2013b) Processes Forming Daily Lamination in a Microbe-Rich Travertine Under Low Flow Condition at the Nagano-yu Hot Spring, Southwestern Japan. *Geomicrobiology Journal*, **30**, 910–927.

O'Reilly, S.S., **Mariotti, G.**, **Winter, A.R.**, **Newman, S.A.**, **Matys, E.D.**, **McDermott, F.**, **Pruss, S.B.**, **Bosak, T.**, **Summons, R.E.** and **Klepac-Ceraj, V.** (2017) Molecular biosignatures reveal common benthic microbial sources of organic matter in ooids and grapestones from Pigeon Cay, The Bahamas. *Geobiology*, **15**, 112–130.

Pantke, C., **Obst, M.**, **Benzerara, K.**, **Morin, G.**, **Ona-Nguema, G.**, **Dippon, U.** and **Kappler, A.** (2012) Green Rust Formation during Fe(II) Oxidation by the Nitrate-Reducing Acidovorax sp. Strain BoFeN1. *Environmental Science & Technology*, **46**, 1439–1446.

Parenteau, M.N. and **Cady, S.L.** (2010) Microbial biosignatures in iron-mineralized phototrophic mats at chocolate pots hot springs, Yellowstone National Park, United States. *PALAIOS*, **25**, 97–111.

Peng, X. and **Jones, B.** (2013) Patterns of biomediated CaCO3 crystal bushes in hot spring deposits. *Sedimentary Geology*, **294**, 105–117.

Perri, E., **Manzo, E.** and **Tucker, M.E.** (2012) Multi-scale study of the role of the biofilm in the formation of minerals and fabrics in calcareous tufa. *Sedimentary Geology*, **263–264**, 16–29.

Potter-McIntyre, S.L., **Williams, J.**, **Phillips-Lander, C.** and **O’Connell, L.** (2017) Taphonomy of Microbial Biosignatures in Spring Deposits: A Comparison of Modern, Quaternary, and Jurassic Examples. *Astrobiology*, **17**, 216–230.

Probst, A.J., **Castelle, C.J.**, **Singh, A.**, **Brown, C.T.**, **Anantharaman, K.**, **Sharon, I.**, **Hug, L.A.**, **Burstein, D.**, **Emerson, J.B.**, **Thomas, B.C.** and **Banfield, J.F.** (2017) Genomic resolution of a cold subsurface aquifer community provides metabolic insights for novel microbes adapted to high CO2 concentrations. *Environmental Microbiology*, **19**, 459–474.

Probst, A.J., **Elling, F.J.**, **Castelle, C.J.**, **Zhu, Q.**, **Elvert, M.**, **Birarda, G.**, **Holman, H.-Y.N.**, **Lane, K.R.**, **Ladd, B.**, **Ryan, M.C.**, **Woyke, T.**, **Hinrichs, K.-U.** and **Banfield, J.F.** (2020) Lipid analysis of CO 2 -rich subsurface aquifers suggests an autotrophy-based deep biosphere with lysolipids enriched in CPR bacteria. *The ISME Journal*, **14**, 1547–1560.

Probst, A.J., **Weinmaier, T.**, **Raymann, K.**, **Perras, A.**, **Emerson, J.B.**, **Rattei, T.**, **Wanner, G.**, **Klingl, A.**, **Berg, I.A.**, **Yoshinaga, M.**, **Viehweger, B.**, **Hinrichs, K.-U.**, **Thomas, B.C.**, **Meck, S.**, **Auerbach, A.K.**, **Heise, M.**, **Schintlmeister, A.**, **Schmid, M.**, **Wagner, M.**, **Gribaldo, S.**, **Banfield, J.F.** and **Moissl-Eichinger, C.** (2014) Biology of a widespread uncultivated archaeon that contributes to carbon fixation in the subsurface. *Nature Communications*, **5**, 5497.

Reitner, J., **Langsford, N.** and **Kruse, P.D.** (2017) An unusual ferruginous-calcitic Frutexites microbialite community from the lower Cambrian of the Flinders Ranges, South Australia. *PalZ*, **91**, 1–3.

Roberts, J.J. and **Stalker, L.** (2017) What have We Learned about CO2 Leakage from Field Injection Tests? *Energy Procedia*, **114**, 5711–5731.

Schumacher, M., **Christl, I.**, **Scheinost, A.C.**, **Jacobsen, C.** and **Kretzschmar, R.** (2005) Chemical Heterogeneity of Organic Soil Colloids Investigated by Scanning Transmission X-ray Microscopy and C-1s NEXAFS Microspectroscopy. *Environmental Science & Technology*, **39**, 9094–9100.

Shipton, Z.K., **Evans, J.P.**, **Kirschner, D.**, **Kolesar, P.T.**, **Williams, A.P.** and **Heath, J.** (2004) Analysis of CO2 leakage through 'low-permeability' faults from natural reservoirs in the Colorado Plateau, east-central Utah. *Geological Society, London, Special Publications*, **233**, 43–58.

Shiraishi, F., **Bissett, A.**, **Beer, D. de**, **Reimer, A.** and **Arp, G.** (2008) Photosynthesis, Respiration and Exopolymer Calcium-Binding in Biofilm Calcification (Westerhöfer and Deinschwanger Creek, Germany). *Geomicrobiology Journal*, **25**, 83–94.

Shiraishi, F., **Nakao, K.**, **Takashima, C.**, **Kano, A.** and **Itai, T.** (2018) Fe(II) oxidation processes at the surface of bacterially colonized iron deposits. *Chemical Geology*, **476**, 161–170.

Suarez-Gonzalez, P. and **Reitner, J.** (2021) Ooids forming in situ within microbial mats (Kiritimati atoll, central Pacific). *bioRxiv*, 2021.05.05.442839.

Takashima, C., **Kano, A.**, **Naganuma, T.** and **Tazaki, K.** (2008) Laminated Iron Texture by Iron-Oxidizing Bacteria in a Calcite Travertine. *Geomicrobiology Journal*, **25**, 193–202.

Takashima, C., **Okumura, T.**, **Nishida, S.**, **Koike, H.** and **Kano, A.** (2011a) Bacterial symbiosis forming laminated iron-rich deposits in Okuoku-hachikurou hot spring, Akita Prefecture, Japan. *Island Arc*, **20**, 294–304.

Takashima, C., **Okumura, T.**, **Nishida, S.**, **Shimamoto, T.**, **Koike, H.** and **Kano, A.** (2011b) Microbial Control on Lamina Formation in a Travertine of Crystal Geyser, Utah. In: *Advances in Stromatolite Geobiology*, Springer, *Joachim Reitner, Nadia-Valérie Quéric, Gernot Arp*, Berlin, Heidelberg, 131, 123–133.

Tourney, J. and **Ngwenya, B.T.** (2008) Bacterial EPS as a mediator of calcium carbonate morphology and polymorphism. *Mineralogical Magazine*, **72**, 291–291.

Tourney, J. and **Ngwenya, B.T.** (2009) Bacterial extracellular polymeric substances (EPS) mediate CaCO3 morphology and polymorphism. *Chemical Geology*, **262**, 138–146.

Trias, R., **Ménez, B.**, **le Campion, P.**, **Zivanovic, Y.**, **Lecourt, L.**, **Lecoeuvre, A.**, **Schmitt-Kopplin, P.**, **Uhl, J.**, **Gislason, S.R.**, **Alfreðsson, H.A.**, **Mesfin, K.G.**, **Snæbjörnsdóttir, S.Ó.**, **Aradóttir, E.S.**, **Gunnarsson, I.**, **Matter, J.M.**, **Stute, M.**, **Oelkers, E.H.** and

Gérard, E. (2017) High reactivity of deep biota under anthropogenic CO2 injection into basalt. Nat Commun. doi: 10.1038/s41467-017-01288-8

Trouwborst, R.E., **Johnston, A.**, **Koch, G.**, **Luther, G.W.** and **Pierson, B.K.** (2007) Biogeochemistry of Fe(II) oxidation in a photosynthetic microbial mat: Implications for Precambrian Fe(II) oxidation. *Geochimica et Cosmochimica Acta*, **71**, 4629–4643.

van Vuuren, D.P., **Hof, A.F.**, **van Sluisveld, M.A.E.** and **Riahi, K.** (2017) Open discussion of negative emissions is urgently needed. *Nature Energy*, **2**, 902–904.

Walter, L.M. (1985) Relative Efficiency of Carbonate Dissolution and Precipitation During Diagenesis: A Progress Report on the Role of Solution Chemistry. doi: 10.2110/pec.86.38.0001

Waltham, T. (2001) Crystal Geyser – Utah's cold one. *Geology Today*, **17**, 22–24.

Ward, L.M., **Idei, A.**, **Terajima, S.**, **Kakegawa, T.**, **Fischer, W.W.** and **McGlynn, S.E.** (2017) Microbial diversity and iron oxidation at Okuoku-hachikurou Onsen, a Japanese hot spring analog of Precambrian iron formations. *Geobiology*, **15**, 817–835.

Webb, S.M. (2005) SIXPack a Graphical User Interface for XAS Analysis Using IFEFFIT. *Physica Scripta*, 1011.

Weiss, J.V., **Rentz, J.A.**, **Plaia, T.**, **Neubauer, S.C.**, **Merrill-Floyd, M.**, **Lilburn, T.**, **Bradburne, C.**, **Megonigal, J.P.** and **Emerson, D.** (2007) Characterization of Neutrophilic Fe(II)-Oxidizing Bacteria Isolated from the Rhizosphere of Wetland Plants and Description of Ferritrophicum radicicola gen. nov. sp. nov., and Sideroxydans paludicola sp. nov. *Geomicrobiology Journal*, **24**, 559–570.

Wilkinson, M., **Gilfillan, S.M.V.**, **Haszeldine, R.S.** and **Ballentine, C.J.** (2009) Plumbing the depths – testing natural tracers of subsurface CO2 origin and migration, Utah, USA. In: *Carbon Dioxide Sequestration in Geological Media—State of the Science*, 619–634.

Supplementary data for:

Carbonate polymorphism controlled by microbial iron redox dynamics at a natural CO_2 leakage site (Crystal Geyser, Utah)

Julie Cosmidis, Shane O'Reilly, Eric T. Ellison, Katherine L. Crispin, David Diercks and Alexis S. Templeton

Table of contents

Supplementary figures

Supplementary Table

Supplementary Text:

Supplementary Figures

Figure S1. Additional pictures of the Crystal Geyser field site. (A,B) Green microbial mats at the surface of the travertine. (C-E) Cauliflower-shaped carbonate structures. (F) Carbonate toroids. (G-I) Calcified bubbles. (J,K) Plants and objects encrusted by rapidly precipitating carbonates.

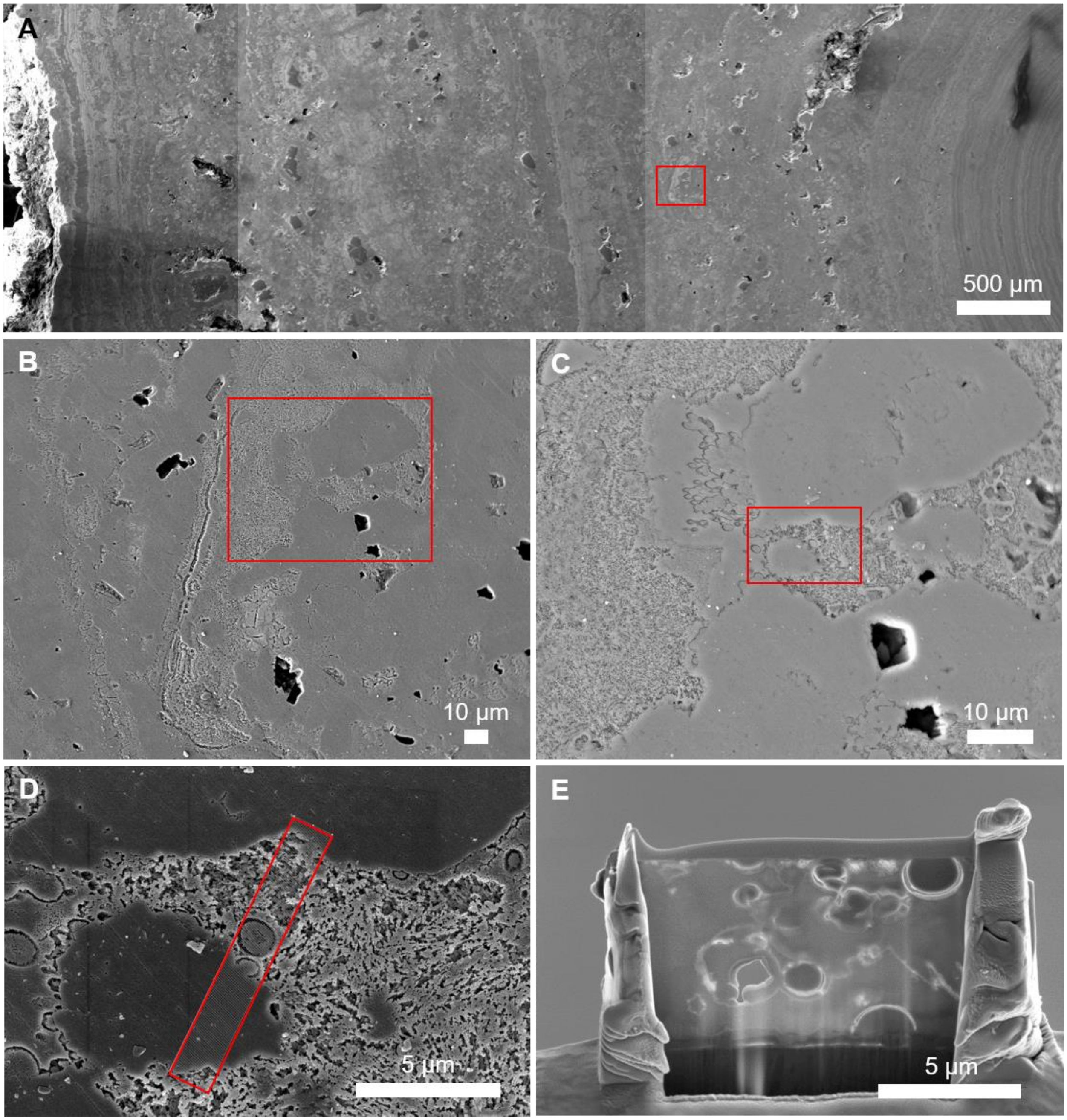

Figure S2. Location of FIB section 1. (A) Low-magnification SEM montage. The border of the pisoid is visible on the left side of the image. The red rectangles on (A), (B) and (C) show the locations of close-ups shown in the subsequent images. The rectangle in (D) indicates where FIB section 1 was milled. (E) SEM image of FIB section 1 after thinning.

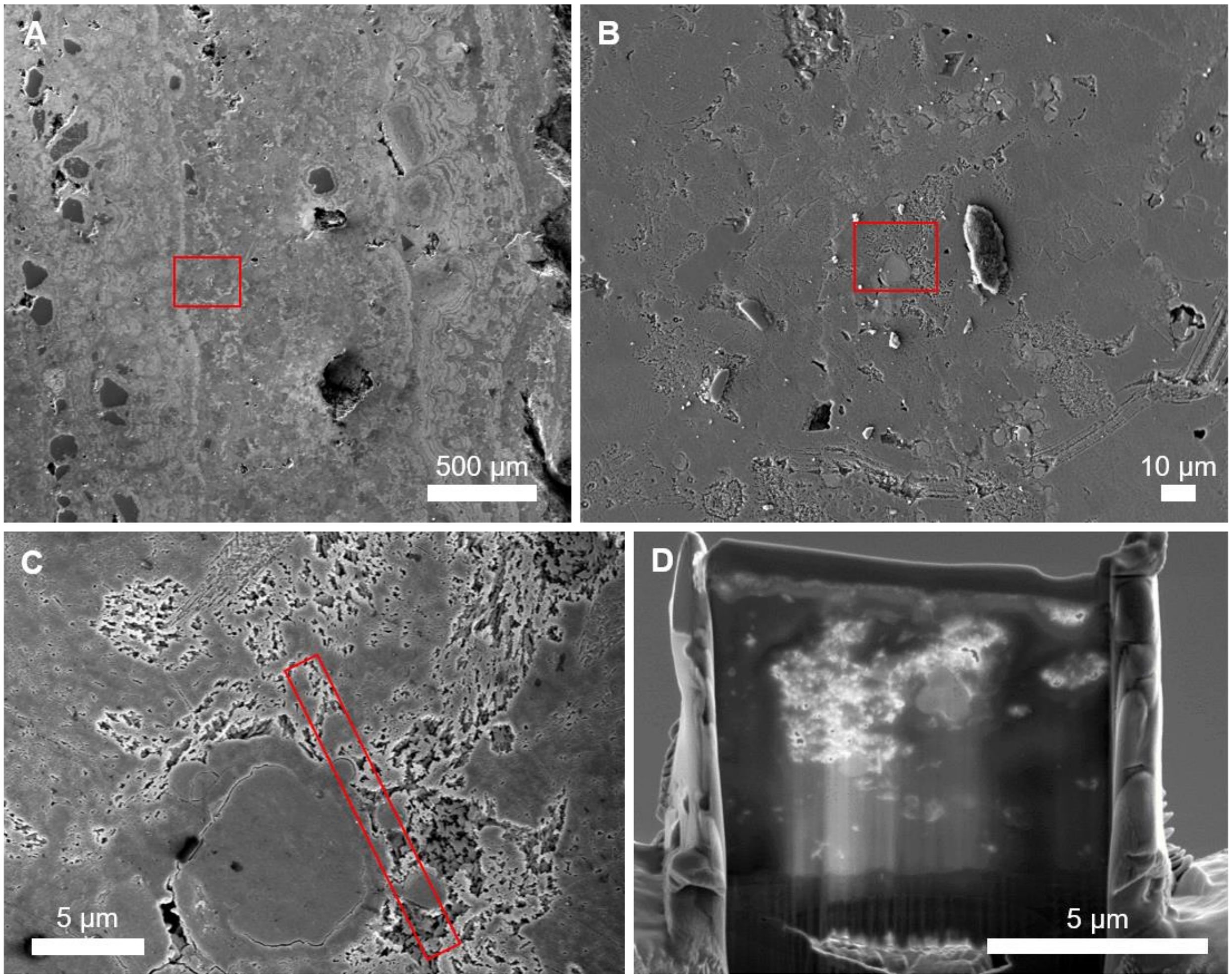

Figure S3. Location of FIB section 2. (A) Low-magnification SEM image. The border of the pisoid is visible on the right side of the image. The red rectangles in (A) and (B) correspond close-ups shown in (B) and (C), respectively. The rectangle in (C) indicates where FIB section 2 was milled. (D) SEM image of FIB section 2 after thinning.

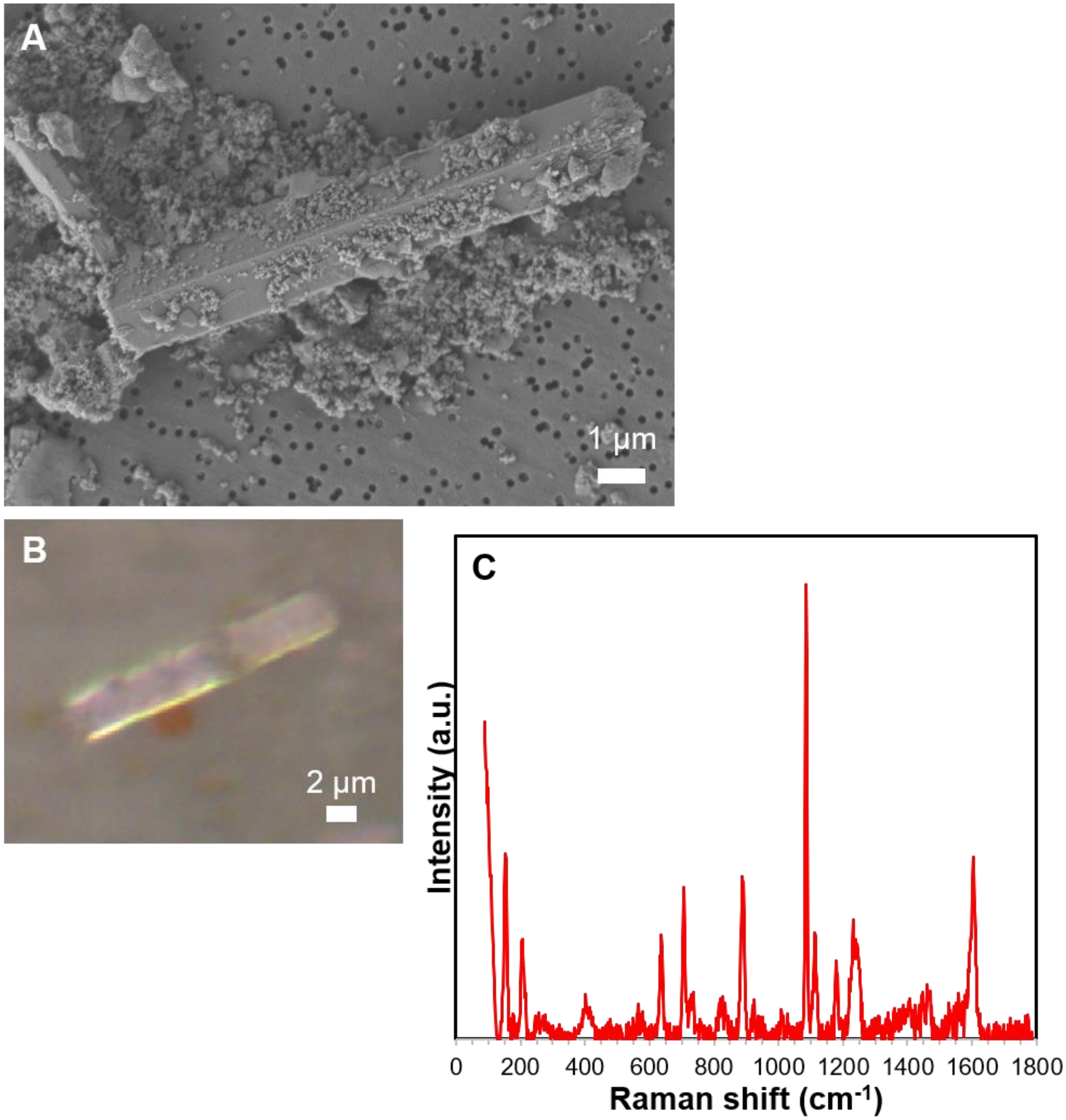

Figure S4. Aragonite particles samples from Crystal Geyser's vent. (A) SEM image. Fine-grained iron minerals are also visible on and around the aragonite blade. (B) Light micrograph. (C) Raman spectrum (corresponding to aragonite).

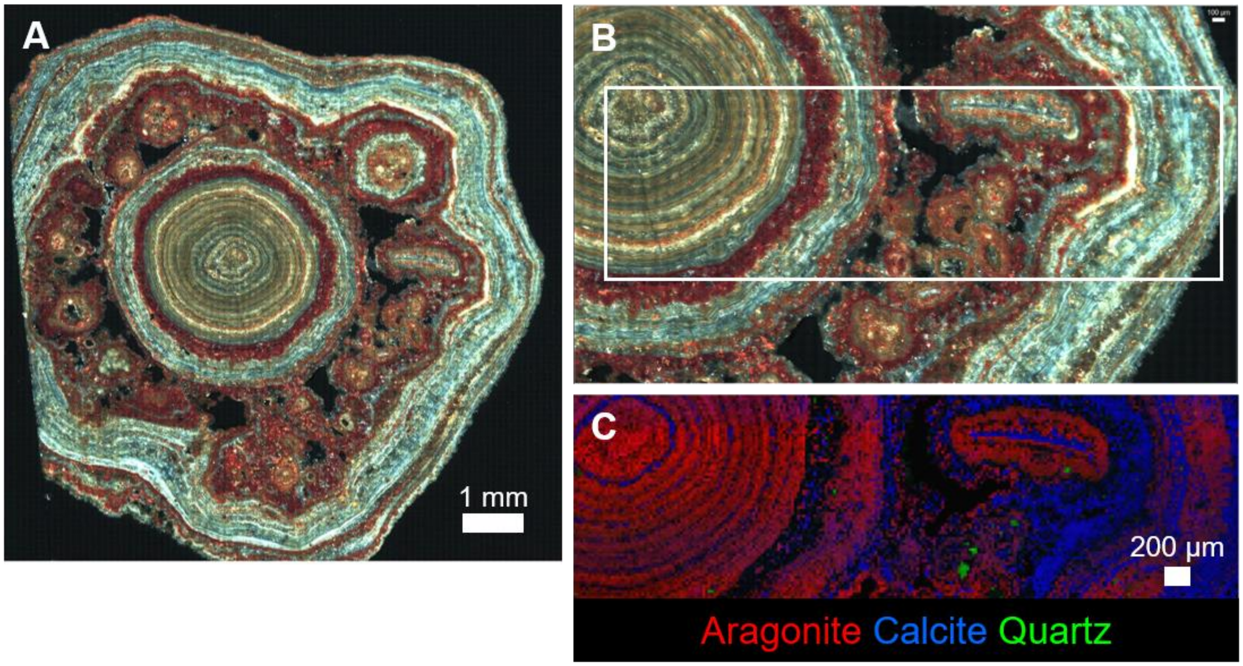

Figure S5. Micrographs and Raman map of a complex pisoid. (A) Montage of cross-polarized light micrographs. (B) Close-up showing the location of the Raman map (white rectangle). (C) Raman map showing the distribution of aragonite (red), calcite (blue) and quartz (green).

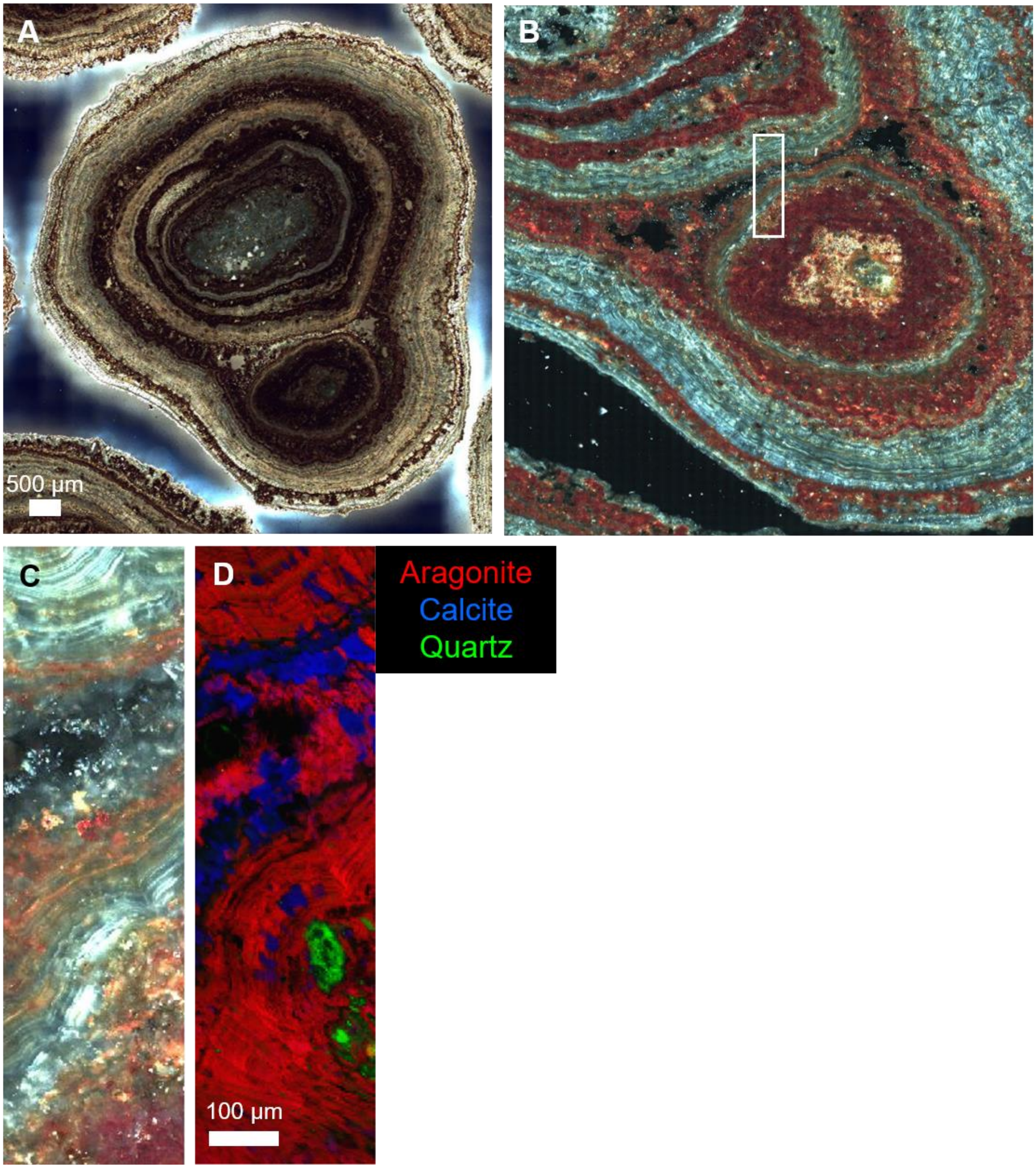

Figure S6. Micrographs and Raman map of a pisoid. (A) Montage of cross-polarized light micrographs. (B) Close-up in cross-polarized light showing the location of the Raman map (white rectangle). (C) Cross-polarized micrograph corresponding to the Raman map location. (D) Raman map showing the distribution of aragonite (red), calcite (blue) and quartz (green).

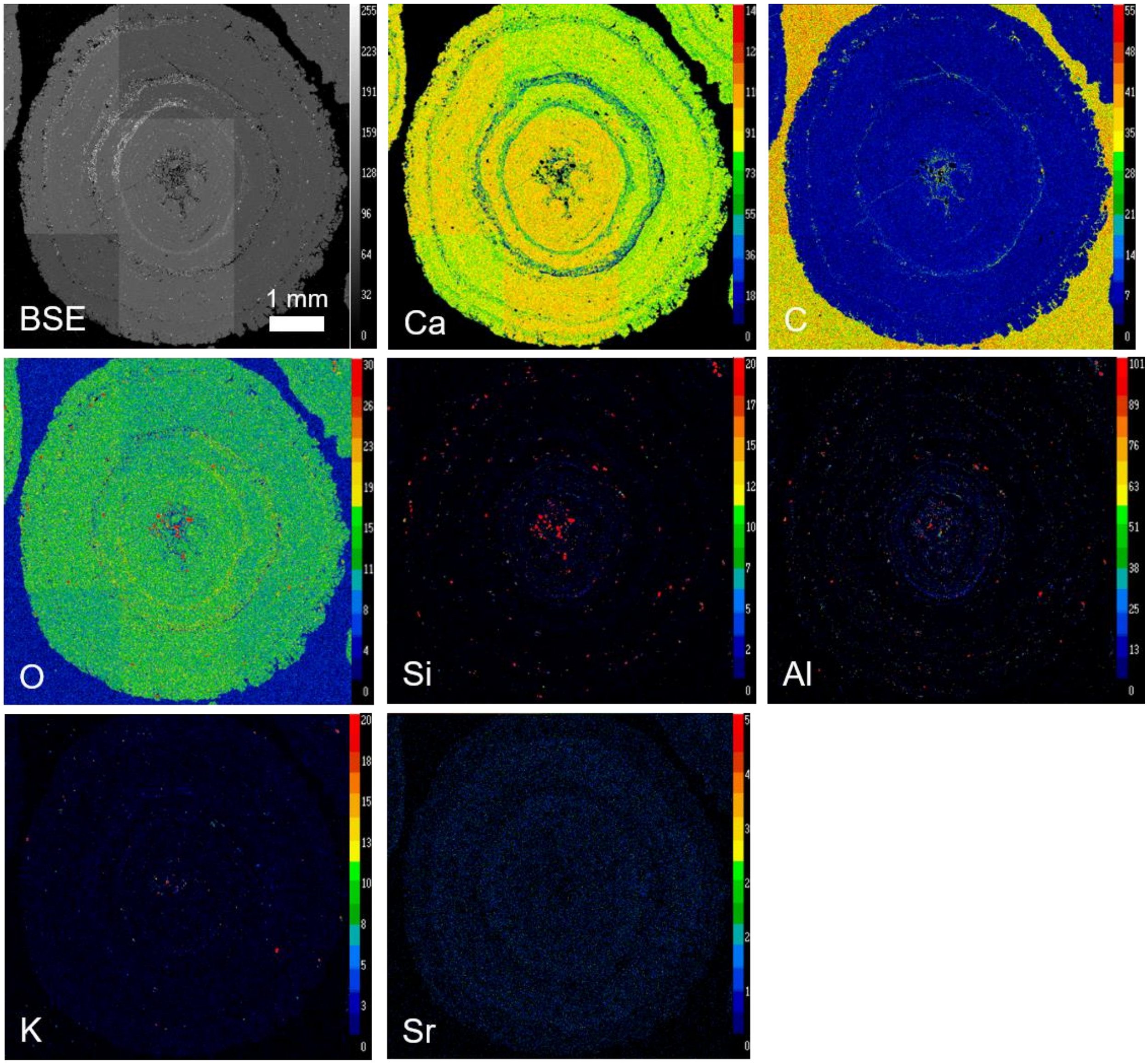

Figure S7. Montages of backscattered electron (BSE) images and additional EPMA maps of a pisoid. See also Figure 4C-E for maps of Fe, Mg and S. The color scales represent relative abundances of the different elements in the sample, but the number indicated on the scales are arbitrary (no calibration has been performed). High abundances of C and O in the background, as well as in porous areas of the pisoid, are due to the embedding epoxy resin used to prepare the thin section.

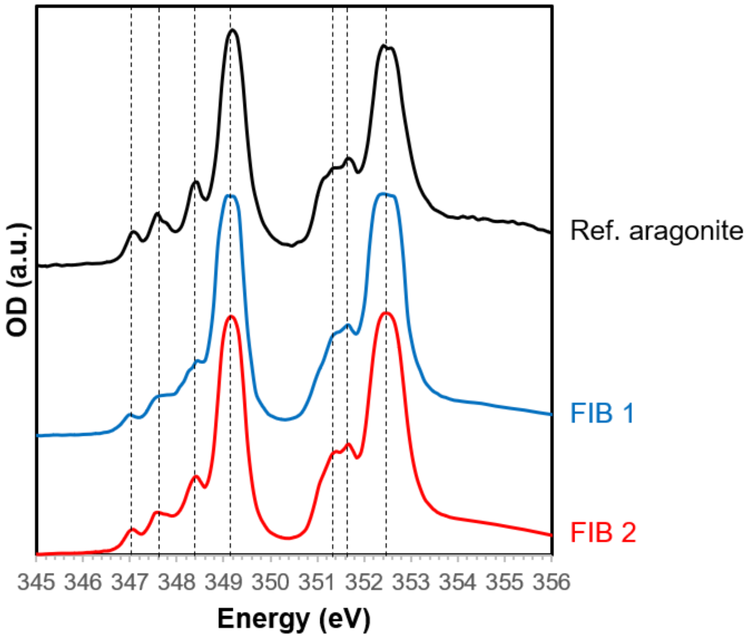

Figure S8. Ca $L_{2,3}$-edge XANES spectra acquired in STXM on the calcium carbonate phase of FIB sections 1 and 2. Dashed vertical lines show the positions of the main peaks and shoulders in the spectrum of a reference aragonite shown for comparison.

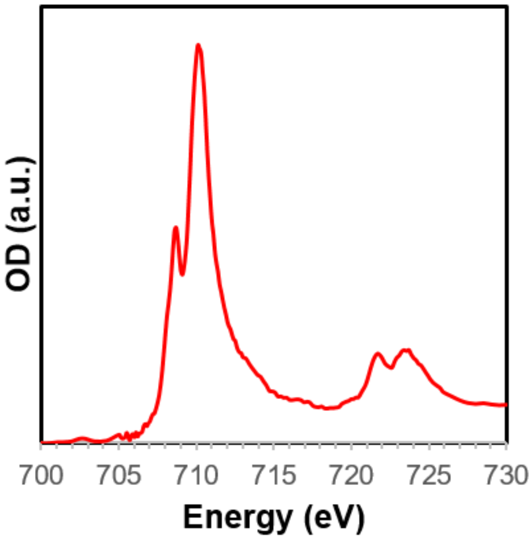

Figure S9. Fe $L_{2,3}$-edge XANES spectrum representative of Fe-rich areas in FIB sections 1 and 2, showing that Fe is present as Fe(III).

Supplementary Table

	Pisoid		**Travertine TL**		**Travertine TB**		**Source**
	Free	Bound	Free	Bound	Free	Bound	
Fatty acids (%)							
14		2.8		4.5	0.7	1.8	Mixed
i15		0.6		1.8	0.1	1.6	Bacteria
a15		0.2		0.7	0.1	1.3	Bacteria
15	3.2	0.6		0.5	0.2	0.6	Mixed
i16		0.2		0.6		0.7	Bacteria
16:1ω9		0.8		1.4	0.8	5.0	Mixed
16:1ω7		0.4					Mixed
16	69.3	52.1	9.4	42.4	7.5	40.0	Mixed
me-16							Bacteria
i17		0.2		0.7	0.1	0.5	Bacteria
a17		0.2		0.5	0.1	0.3	Bacteria
17	1.1	0.5		0.6	0.2	0.6	Bacteria
phytanic		0.2		0.2			Chlorophyll degradation product
18:1ω11c					2.6		
18:1ω9c		0.8	43.6	2.4	34.7		Green algae, other microalgae
18:1ω7c					17.7		Bacteria
18:1ω9t		1.2	23.7	3.1	13.9	1.2	
18:1ω7t					1.5		
18	13.5	30.7	5.7	18.1	7.4	26.9	Mixed
19					0.1		Mixed
20:1ω9c					7.1		Microeukaryotes
20:1ω9t					2.5		Microeukaryotes
20	3.7	0.8	1.7	2.0	0.7	1.3	
21		0.2		0.8	0.1	0.5	
22:1ω9c			2.1		0.8		Microeukaryotes
22	5.2	0.8	4.5	4.5	0.2	1.4	Algae, higher plants
23		0.2	0.3	0.6		0.6	Algae, higher plants
24	10.8	3.7	5.5	6.8	0.7	12.1	Algae, higher plants
25		0.3	0.3	0.5		0.4	Algae, higher plants
26	2.8	0.7	2.4	4.0	0.2	2.5	Higher plants, algae
27		0.2		0.3		0.2	Higher plants, algae
28	1.2	0.7	0.8	1.7		0.4	Higher plants, algae
29		0.1		0.2			Higher plants, algae
30		0.8		1.2			Higher plants, algae
Σ (ng g^{-1})	*375*	*1525*	*887*	*1210*	*1657*	*383*	
(Algae+Plant)/Bacteria	*5.5*	*4.0*		*4.6*	*2.5*	*3.4*	
3-hydroxy acids							

12		5		3		17	Bacteria (possibly anaerobic)
14		22		20		17	Bacteria (possibly anaerobic)
i15		7		10		8	Bacteria (possibly anaerobic)
a15		2		3			Bacteria (possibly anaerobic)
15		1		1			Bacteria (possibly anaerobic)
i16	18	8		1		7	Bacteria (possibly anaerobic)
a16				5			Bacteria (possibly anaerobic)
16	20	23		17		16	Bacteria (possibly anaerobic)
i17	39	23		21	43	18	Bacteria (possibly anaerobic)
a17	23	6		6	14	7	Bacteria (possibly anaerobic)
17		1		1			Bacteria (possibly anaerobic)
i18				1			Bacteria (possibly anaerobic)
18		7		14	42	9	Bacteria (possibly anaerobic)
Σ (ng g^{-1})	*52*	*25*	*n.d.*	*104*	*15*	*16*	
Monoalkylglycerol ethers (MGM)							
i15				15			Bacteria (likely aquatic, anaerobic)
a15				1			Bacteria (likely aquatic, anaerobic)
15				2			Bacteria (likely aquatic, anaerobic)
i16				3			Bacteria (likely aquatic, anaerobic)
16:1				3			Bacteria (likely aquatic, anaerobic)
16				24	100		Bacteria (likely aquatic, anaerobic)
me-16				13			Bacteria (likely aquatic, anaerobic)
me-16				10			Bacteria (likely aquatic, anaerobic)
i17				2			Bacteria (likely aquatic, anaerobic)
a17				3			Bacteria (likely aquatic, anaerobic)
17				2			Bacteria (likely aquatic, anaerobic)
me-17				2			Bacteria (likely aquatic, anaerobic)
i18							Bacteria (likely aquatic, anaerobic)
a18							Bacteria (likely aquatic, anaerobic)
18:1				2			Bacteria (likely aquatic, anaerobic)
18				7			Bacteria (likely aquatic, anaerobic)
me-18							Bacteria (likely aquatic, anaerobic)
i19				7			Bacteria (likely aquatic, anaerobic)
19:1				3			Bacteria (likely aquatic, anaerobic)
19							Bacteria (likely aquatic, anaerobic)
Σ (ng g^{-1})				*19*	*2*		
n-alkanols (%)							
16				1.6	13.3		Microalgae
17					0.4		Microalgae
18	1.4			2.4	21.4	76.8	Microalgae
20	0.6	4.1		0.7	1.7		Microalgae
21							Microalgae
22	1.1	3.1	0.5	0.9	1.9	23.2	Microalgae

24	1.8	6.7	1.0	1.5	3.0		Microalgae, higher plants
26	2.4	10.1	1.1	3.1	1.8		Microalgae, higher plants
Nonacosan-12-ol	24.2		22.9	11.3	40.5		Higher plants (related to *Tamarix* sp.)
28	2.6	7.7	1.3	1.8	1.3		Higher plants
Hentriacontan-12-ol	63.4	61.9	73.1	75.7	14.2		Higher plants (related to *Tamarix* sp.)
30	2.4	6.5		1.1	0.5		Higher plants
Σ (ng g^{-1})	*91*	*<1*	*130*	*10*	*19*	*<1*	
Higher Plant/Algae	*31*	*12*	*185*	*17*	*2*	*0*	
Ratio Alkan-12-ols	*2.6*		*3.2*	*6.7*	*0.4*		Different plant input, or diagenetic stability of C31 vs C29
Sterols (%)							
lanosterol					2.3		
cholesterol	36.2	33.6	12.0	5.4	6.8		Microeukaryotes, microalgae
cholestanol	3.2		5.2	8.7	6.9		degradation product of cholesterol
campesterol	3.6		9.1	6.5	1.1		Algae (diatoms, green algae), higher plants
stigmasterol	24.0	33.4	58.4	61.8	68.0	100.0	Algae (diatoms, green algae), higher plants
22-ethyl-coprostenol					11.5		degradation product of stigmasterol?
β-sitosterol	30.3	33.0	12.9	13.3	4.4		Algae (diatoms, green algae), higher plants
sitostanol	2.8		2.4	4.4	1.3		degradation product of β-sitosterol
Σ (ng g^{-1})	*737*	*16*	*468*	*73*	*242*	*19*	
stanol/stenol	*0.1*	*0.0*	*0.3*	*0.7*	*0.7*		more reducing environmental, higher anaerobic activity?
cholest/stigmast	*1.5*	*1.0*	*0.2*	*0.1*	*0.1*		greater eukaryote heterotrophic activity
stigmasterol/sitosterol	*0.8*	*1.0*	*4.5*	*4.7*	*15.5*		differences in photosynthetic community
Hydrocarbons							
2,2-dime-C16	0	0	0	0	32	0	Cyanobacteria?
23	6	0	0	0	13	0	Algae, higher plants
24	4	4	0	5	6	0	Algae, higher plants
25	9	8	10	9	9	17	Higher plants, algae
26	6	13	5	7	3	0	Higher plants
27	12	16	22	14	8	31	Higher plants
28	7	15	6	8	2	0	Higher plants
29	25	18	32	31	15	36	Higher plants
30	7	11	5	7	6	0	Higher plants
31	19	10	20	16	6	16	Higher plants
32	5	5	0	3	1	0	Higher plants
Σ (ng g^{-1})	*298*	*38*	*141*	*17*	*51*	*6*	
Higher Plant/Algae	*8*	*21*		*17*	*1*		
Other (ng g^{-1})							
Archaeol	294						Archaea
Total							
Σl lipids (ng g^{-1})	*1847*	*1605*	*1627*	*1432*	*1988*	*424*	

Table S1. Free and carbonate-bound lipids in Crystal Geyser pisoids and travertines.

Supplementary Text: Detailed interpretation of lipid analyses

Fatty acids, ranged from 14 to 30 carbon chain lengths, were a major lipid component in all samples. Monounsaturated and methyl-branched (typically *iso* and *anteiso* chain positions) were present as well as *n*-saturated fatty acids. The highest abundances of fatty acids were observed in the bound lipid pools of the pisoids and travertine TL. Some of these fatty acids (especially *n*-saturated and monounsaturated) are common to both bacteria and eukaryote domains, so there is some uncertainty in source assignment. Methyl-branched fatty acids are primarily sourced from bacteria (Kaneda, 1991). 3-hydroxy acids were also identified in relatively minor amounts in all samples apart from the free lipid pool of travertine TL. Carbon chain lengths ranged from 12 to 18, and methyl-branched isomers were a major component, particularly *iso*- and *anteiso*-heptadecanoic acid. These are derived from gram negative bacteria bacteria, as components of lipopolysaccharides, and are often associated with anaerobic heterotrophic bacteria (Rietschel, 1976; Wang *et al.*, 2016).

Monoalkyl glycerol monoethers (MGM) were present in minor amounts in the bound lipid fraction of travertine TL and in the free lipid fraction of travertine TB. These are bacterial lipids, and based on current evidence are particularly common in aquatic extremophiles and heterotophic mesophiles engaged in sulfur cycling (particularly sulfate reduction) (Rütters *et al.*, 2001; Hernandez-Sanchez *et al.*, 2014). MGM are rarely reported in non-aquatic settings, and a large contribution from methyl-branched members is indicative of sedimentary (probably sub-oxic/anoxic) bacteria rather than aerobic aquatic bacteria. The presence of MGM in the travertines and their absence in the pisoids suggest that the microbial communities present during precipitation of pisoids and travertine minerals are different.

n-alkan-1-ols between 12 and up to 24 carbon chain lengths are majorly associated with photosynthetic microalgae, while *n*-alkan-1-ols between about 24 and 32 carbon chain lengths are majorly associated with higher plants (Pancost & Boot, 2004; Volkman, 2006). Long chain *n*-alkan-12-ols are rarely reported and appear to be quite restricted to cuticular wax lipids from *Tamarix*-type species (Basas-Jaumandreu *et al.*, 2014), which are abundant in the region of Crystal Geyser. As such these likely reflect aeolian-sourced inputs. Minor amounts of alkan-12-ols were identified in all free and bound lipid fractions, although the abundance in the bound lipid fractions was generally over an order of magnitude lower. Interestingly the ratio of hentriacontan-12-ol to nonacosan-12-ol was quite varied (0.4 to 6.7, Table S1). Assuming, similar degradation rates, this indicates distinct differences in the input of different vascular plant species and/or pathways between samples.

Sterols were abundant in all free lipid fractions, and are diagnostic for higher plants and microalgae (Volkman *et al.*, 1998; Volkman, 2006). These likely reflect aeolian input from regional vascular plants and photosynthetic microalgal biomass. Cholesterol is the sole sterol in animals and heterotrophic microeukaryotes, as well as a relatively minor sterol in certain photosynthetic microalgae. The presence of cholesterol amounts similar to C_{29} sterols likely reflects input from heterotrophic microeukaryotes such as protists. Cholesterol was a major sterol in pisoids samples and likely reflect aquatic protists. High concentrations of stanols relative to stenols is generally indicative of reducing environments and significantly anaerobic bacterial hydrogenation reactions (Wakeham, 1989). Cholestanol/cholesterol ratios for the pisoids are <0.1, 0.5 for TB FL fraction, and > 1.0 for TL BL and TB FL. Thus, while the absence of sterols in bound lipid fractions may be related to low original concentrations, it may also reflect microbial activity under reducing conditions during mineral precipitation.

Hydrocarbons were identified in the free lipid fractions of all samples, and were dominated by long chain odd carbon number *n*-alkanes, particularly heptacosane, nonacosane and hentricontane. This is strong evidence of vascular plant wax lipid input (Eglinton & Hamilton, 1967; Bush & McInerney, 2013). One methyl-branched alkane was found in the free lipid pool of travertine TB. This is tentatively identified as 2,2-dimethyl-hexadecane and indicates the presence of cyanobacteria (Gomes *et al.*, 2020). Cyanobacterial hydrocarbons were not identified in any other sample, suggesting they play a minor role at Crystal Geyser, apart from a possibly role in mineral precipitation in travertine TB.

Archaeol (di-O-phytanylglycerol) is a membrane lipid found in certain archaea (Kate, 1993). It was found in relatively high abundances in the pisoid free lipid fraction. This most likely reflects aquatic, possibly extremophilic, archaea living in the water close to close to the geyser. The fact that it was not detected in the bound lipid fraction of the pisoids indicates that these archaea are associated with the aqueous phase and as detritus on mineral surfaces but are not closely associated with mineral precipitation in the Crystal Geyser pisoids.

References

Basas-Jaumandreu, J., **López, J.** and **de las Heras, F.X.C.** (2014) Resorcinol and m-guaiacol alkylated derivatives and asymmetrical secondary alcohols in the leaves from Tamarix canariensis. *Phytochemistry Letters*, **10**, 240–248.

Bush, R.T. and **McInerney, F.A.** (2013) Leaf wax n-alkane distributions in and across modern plants: Implications for paleoecology and chemotaxonomy. *Geochimica et Cosmochimica Acta*, **117**, 161–179.

Eglinton, G. and **Hamilton, R.J.** (1967) Leaf Epicuticular Waxes. *Science*, **156**, 1322–1335.

Gomes, M.L., **Riedman, L.A.**, **O'Reilly, S.**, **Lingappa, U.**, **Metcalfe, K.**, **Fike, D.A.**, **Grotzinger, J.P.**, **Fischer, W.W.** and **Knoll, A.H.** (2020) Taphonomy of Biosignatures in Microbial Mats on Little Ambergris Cay, Turks and Caicos Islands. *Frontiers in Earth Science*, **8**, 387.

Hernandez-Sanchez, M.T., **Homoky, W.B.** and **Pancost, R.D.** (2014) Occurrence of 1-O-monoalkyl glycerol ether lipids in ocean waters and sediments. *Organic Geochemistry*, **66**, 1–13.

Kaneda, T. (1991) Iso- and anteiso-fatty acids in bacteria: biosynthesis, function, and taxonomic significance. *Microbiol Rev*, **55**, 288–302.

Kate, M. (1993) Chapter 9 Membrane lipids of archaea. In: *New Comprehensive Biochemistry* (Ed. M. Kates, D.J. Kushner, and A.T. Matheson), *Elsevier*, 26, 261–295.

Pancost, R.D. and **Boot, C.S.** (2004) The palaeoclimatic utility of terrestrial biomarkers in marine sediments. *Marine Chemistry*, **92**, 239–261.

Rietschel, E.T. (1976) Absolute configuration of 3-hydroxy fatty acids present in lipopolysaccharides from various bacterial groups. *Eur J Biochem*, **64**, 423–428.

Rütters, H., **Sass, H.**, **Cypionka, H.** and **Rullkötter, J.** (2001) Monoalkylether phospholipids in the sulfate-reducing bacteria Desulfosarcina variabilis and Desulforhabdus amnigenus. *Arch Microbiol*, **176**, 435–442.

Volkman, J.K. (2006) Lipid Markers for Marine Organic Matter. In: *Marine Organic Matter: Biomarkers, Isotopes and DNA* (Ed. J.K. Volkman), *Springer*, Berlin, Heidelberg, 27–70.

Volkman, J.K., **Barrett, S.M.**, **Blackburn, S.I.**, **Mansour, M.P.**, **Sikes, E.L.** and **Gelin, F.** (1998) Microalgal biomarkers: A review of recent research developments. *Organic Geochemistry*, **29**, 1163–1179.

Wakeham, S.G. (1989) Reduction of stenols to stanols in particulate matter at oxic–anoxic boundaries in sea water. *Nature*, **342**, 787–790.

Wang, C., **Bendle, J.**, **Yang, Y.**, **Yang, H.**, **Sun, H.**, **Huang, J.** and **Xie, S.** (2016) Impacts of pH and temperature on soil bacterial 3-hydroxy fatty acids: Development of novel terrestrial proxies. *Organic Geochemistry*, **94**, 21–31.